

# COLLOIDAL TRANSPORT IN LOCALLY PERIODIC EVOLVING POROUS MEDIA – AN UPSCALING EXERCISE

ADRIAN MUNTEAN <sup>\*</sup> AND CHRISTOS V. NIKOLOPOULOS <sup>†</sup>

**Abstract.** We derive an upscaled model describing the aggregation and deposition of colloidal particles within a porous medium allowing for the possibility of local clogging of the pores. At the level of the pore scale, we extend an existing model for colloidal dynamics including the evolution of free interfaces separating colloidal particles deposited on solid boundaries (solid spheres) from the colloidal particles transported through the gaseous parts of the porous medium. As a result of deposition, the solid spheres grow reducing therefore the space available for transport in the gaseous phase. Upscaling procedures are applied and several classes of macroscopic models together with effective transport tensors are obtained, incorporating explicitly the local growth of the solid spheres. The resulting models are solved numerically and various simulations are presented. In particular, they are able to detect clogging regions, and therefore, can provide estimates on the storage capacity of the porous matrix.

**Key words.** Evolving porous media, Colloidal dynamics, Clogging, Storage capacity, Asymptotic homogenization, Numerical simulations.

**AMS subject classifications.** Primary 35B27, 76M50; Secondary 76R50, 76VXX, 76M10

**1. Introduction.** We investigate the effect the motion, aggregation, fragmentation and deposition of colloidal particles through porous materials have on effective transport properties. Colloids are very small particles (from 1 to 100 nm) that play nowadays a very important role in the success of biological and technological applications, like waste water treatment, food industry, 3D printing, drug-delivery design, etc. A mathematically interesting aspect which complicates also the physics of the situation is that colloids like to aggregate and build large clusters which then fragmentate if some critical thresholds are met. We refer the reader to, for instance, [13, 33, 35], and [42] for more details on the mathematical modelling of the aggregation and coagulation processes.

The main subject of this work is to extend the modelling approach presented in [20, 21] (see also in the references cited therein) to include the gradual increase of the solid skeleton of the porous medium due to colloids deposition via a moving boundary modelling strategy. More specifically, we model a reaction-diffusion system operating within a porous medium consisting of colloidal aggregates of varying size. These aggregates (populations of clusters) interact with each other and with the porous matrix. As main effect of the colloidal aggregation and of the deposition of the large clusters within the evolving porous network, either the transport, or the storage capacity or both are reduced. To explore the multiscale factors behind this effect, we wish to capture *how* the local blocking of the pores (the so-called *pore clogging*) affects the effective transport and storage. The clogging effect will be pointed out in terms of closed-form formulas for all effective coefficients. Obtaining quantitatively correct entries in the tortuosity tensor requires a deep understanding on how ink-

---

<sup>\*</sup> Department of Mathematics and Computer Science, Karlstad University, Sweden (adrian.muntean@kau.se).

<sup>†</sup> Department of Mathematics, University of the Aegean, Gr-83200 Karlovassi, Samos, Greece. (cnikolo@aegean.gr).

bottle pores and blind pores become closed pores or on how through pores clog due to a heterogeneous deposition of colloids. Under some assumptions, these entries will be obtained in this framework through a locally-periodic homogenization asymptotics as in [7, 15, 45] combined with a suitable matched-asymptotics approach as in [23, 29]. The numerical evaluation of these tensors will illustrate the appearance of clogging. The situation remotely resembles the filter blockage case discussed in [11]. Using a similar methodology as in [20], one can also point out the effect of a nonlinear dynamic blocking function on the colloidal deposition.

It is worth noting that such investigations of the occurrence of clogging are relevant in a number of engineering directions, especially as *multiscale storage* of unwanted particles (chemical species, defects, mechanical damage, etc. ) is concerned. For instance, the efficient and safe storage of injected supercritical carbon dioxide (CO<sub>2</sub>) underground is now one potential solution for reducing CO<sub>2</sub> emissions in the atmosphere; see e.g. [39] or [30]. Interface and grain boundaries have shown to be ideal sinks for radiation-induced defects. Especially in nano-structured materials, such interfaces can become ideal places for Helium storage; compare e.g. [5, 46]. Yet another typical research field fitting well this problem setting is filtration combustion [41]. As one can expect after weighing the number of mathematical difficulties in handling simultaneously the multiscale (often stochastic) structure of the material, the motion of the many microscopic interfaces, the strong coupling and the involved nonlinearities in the physical and chemical process of the setting, there is not yet a consensus on how to approach the question of averaging reactive, actively evolving porous media. A couple of attempts have been successful in dealing with particular moving interface scenarios. Concerning the employed mathematical techniques, we refer the reader to averaging approaches involving a direct use of suitable level set equations (cf. e.g. [36, 37, 38]), phase field equations (cf. e.g. [12]), direct handling of the moving boundary motion e.g. by a precise accounting of free-interfaces-induced volume changes (cf. e.g. [32]), or of local balance laws written in terms of a time and space-dependent porosity seen as an intensive quantity (cf. e.g. [6, 10, 44]).

Summarizing, in the present work we derive an upscaled model describing the aggregation and deposition of colloidal particles within a porous medium with growing spheres as internal microstructure. Two upscaling procedures are applied and several classes of macroscopic models together with effective transport tensors are obtained. They all depend on the local growth of the solid spheres. The simulations based on our models allow us to capture the phenomenon of clogging and to estimate a posteriori how much mass can be stored in the porous matrix.

The paper is structured as follows: The geometry of the porous material as well as the setting of the equations for the microscopic (pore-level) model are given in Section 2. Section 3.1 contains the non-dimensionalization of the system, while in Section 4 and in 5 we provide the details of the upscaling procedures for a couple of different scenarios allowing for a locally periodic distribution of pores (perforations) as well as for the possibility of touching of the microstructures. Moreover a finite element scheme for the numerical approximation of the system is presented in Section 6. A couple of numerical simulations illustrate the behavior of the Galerkin approximations of the solution to the upscaled model. The paper concludes with the discussion from Section 7.

**2. The microscopic model.** The colloidal population consists of identical particles called primary particles. They aggregate to bigger shapes and then they fragmentate and finally reach some size, say  $i$ . We refer to each particle of size  $i$  as a

member of the  $i^{\text{th}}$  species (or  $i^{\text{th}}$  cluster). Each colloidal species is characterized by the number of primary particles that it contains. We have in view here only those situations where each considered size contains a huge number of particles. To describe the situation, we introduce the notation  $u_i$  when referring to the population of particles of size  $i$ ,  $i \in \{1, \dots, N\}$  for a fixed choice  $N$ . The value  $N$  corresponds to the biggest allowed size.

*Description of the porous domain.* The porous matrix we have in mind is assumed to have a locally periodic structure as described in Figure 4.1, which resembles the ordered porous medium from [6]. A two-dimensional microstructure approach is adapted here corresponding to a pseudo 3D dimensional geometry, e.g. see Figure 5.1 (This could be reduced to a even simpler and less realistic one-dimensional microstructure approach as in [22]). More precisely,  $\Omega$  is a bounded domain in  $\mathbb{R}^2$  representing our porous material<sup>1</sup>. This is assumed to consist of an infinite number of identical cells, each one corresponding to a single pore of the material. More specifically, for  $\ell > 0$  we take  $Y = \{\sum_{i=1}^2 \lambda_i \vec{e}_i : 0 < \lambda_i < \ell\}$  an  $\ell$ -cell in  $\mathbb{R}^2$  representing a single pore of the material,  $Y_1(x) \subset Y$  open, representing the solid grain and  $Y_0 = Y \setminus \text{clos}(Y_1)$  the rest of the cell. The boundary of  $Y_1(x)$  will be denoted by  $\Gamma(0, x) = \partial Y_1(x)$  and is assumed to be piecewise smooth. As the process evolves, the mobile colloidal species which reach a certain cluster size tend to deposit at the boundary  $\Gamma(0, x)$  of the solid grain  $Y_1(x)$ . The basic picture we have in mind is that the solid grain is a disc of radius  $r$ . As more species deposit on its boundary, its radius gradually increases giving rise to a ball  $B(r)$  with  $Y_1 = B(0) \subset B(r)$ . We use a radially symmetric setting by assuming that the accumulation of the colloidal species upon the solid grain is uniform. We point this out using the notation  $\Gamma = \Gamma(r)$ , meaning in fact  $\Gamma = \Gamma(r(t, x))$ . We also need to emphasize that an additional assumption used in the above setting is that the shape of the colloidal particles (spherical) does not play an important role in the accumulation process. Inclusion of this characteristic together also with gravitational effect for large  $N$  are not taken into account for simplicity reasons.

*Setting of the model equations in the patch  $Y \subset \Omega$ .* As the mobile matter deposits on  $\Gamma(r)$ , the corresponding deposited mass takes up volume and leads to the increase in  $r$ , resulting in a gradual decrease in the porosity of the material, visible at the macroscopic scale. To describe the deposition process we use a linear evolution equation and call  $v$  the mass of all deposited colloidal populations. The mobile species deposited on  $\Gamma(r)$  transform into immobile species via an exchange term in the form of a Henry-type law. This is a simple way of modeling a non-equilibrium deposition process. The approach can be extended by using a non-linear differential equation as the one in [20], especially if one aims to come closer to the experimental data from [18]. Furthermore, each mobile species  $u_i$  is transported by diffusion within the patch  $Y$  of the porous medium  $\Omega$  with a production term expressing the aggregation and fragmentation processes. To fix ideas, we assume that the rate of collision is proportional to the concentration of the colliding species and assume the Smoluchowski ansatz.

---

<sup>1</sup>A similar discussion can be done for the case of  $\Omega \subset \mathbb{R}^3$  with a minimal number of modifications mostly concerning scaling factors.

According to the above description, the model equations have the form:

$$\partial_t u_i = d_i \Delta u_i + R_i(u) \quad \text{in } Y - B(r), i \in \{1, \dots, N\} \quad (2.1)$$

$$-d_i \nabla u_i \cdot n = a_i u_i - b_i v \quad \text{on } \Gamma(r) \quad (2.2)$$

$$\partial_t v = \sum_{i=1}^N (a_i u_i - b_i v) \quad \text{on } \Gamma(r), \quad (2.3)$$

with  $a_i, b_i$  constants of proportionality in Henry's law and  $d_i$  the diffusion coefficient of the species  $i$ . The reaction rate  $R_i(u)$  is here assumed to take the classical Smoluchowski form (see [20]) :

$$R_i(u) = \frac{1}{2} \sum_{i+j=k}^{\infty} \alpha_{i,j} \beta_{i,j} u_i u_j - u_k \sum_{i=1}^{\infty} \alpha_{k,i} \beta_{k,i} u_i, \quad (2.4)$$

with  $u = (u_1, u_2, \dots, u_N)$ . Also  $\beta_{i,j}$  is the collision kernel - rate constant determined by the transport mechanism that bring the particles in close contact,  $\alpha_{i,j} \in [0, 1]$  is the collision efficiency, the fraction of collision that finally form an aggregate ([20]). Note that if we consider only one colloidal species, then this reduces to  $R(u) = -cu^2$ , with a suitable reaction constant  $c > 0$ . As alternative to (2.4),  $R$  can take the Becker-Döring form ([19]).

The growth of the pore radius  $r$  relates naturally to the amount of matter deposited  $v$ . More precisely, the rate of increase of the volume of immobile species is proportional to the rate of change of deposition of  $v$ .

Therefore if the volume occupied by the immobile species located at  $x \in \Omega$  is denoted with  $\mathcal{V}(x, t)$ ,

$$\partial_t \mathcal{V}(x, t) = \rho^{-1} \int_{\Gamma(x, t)} \partial_t v, \quad (2.5)$$

for  $\rho$  the density of the immobile species.

Thus for a two-dimensional radially symmetric setting  $V = \pi r^2$  and for  $r' = \frac{dr}{dt}$ , we have

$$r(t, x) r'(t, x) = \rho^{-1} \frac{1}{2\pi} \int_{\Gamma(t, x)} \partial_t v. \quad (2.6)$$

The model needs to be completed with initial conditions. At the boundary of the patch  $Y$  we consider periodic boundary conditions for  $u_i$ . We will discuss in section 5 the case  $\partial Y \cap \partial \Omega \neq \emptyset$ .

**3. Scaling.** In this section, we choose to work with dimensionless quantities and introduce our notation describing the geometry of the porous material.

**3.1. Nondimensionalization at the patch level.** We set  $t = t_0 \tilde{t}$ ,  $x = \ell \tilde{x}$ ,  $u_i = u_0 \tilde{u}_i$ ,  $v = v_0 \tilde{v}$ . For convenience, the constants  $d_i, a_i, b_i$  can be written in the following way  $d_i = d \tilde{d}_i$ ,  $a_i = a \tilde{a}_i$ ,  $b_i = b \tilde{b}_i$ , for  $d := \max_{i \in \{1, \dots, N\}} \{d_i\}$ ,  $a := \max_{i \in \{1, \dots, N\}} \{a_i\}$ ,  $b := \max_{i \in \{1, \dots, N\}} \{b_i\}$ . Also, we take  $r = \ell \tilde{r}$  and, for convenience, we use further  $r$  instead of  $\tilde{r}$ . The same convention of removing the tilde from  $\tilde{X}$  to yield the scaled quantity  $X$  applies also to our scaled geometry (i.e. when referring to  $\tilde{\Omega}, \tilde{Y}, \tilde{\Gamma}, \tilde{B}(r)$ , etc.).

Regarding equation (2.1), dropping tilde in the process, we obtain

$$\frac{1}{t_0} \partial_t u_i = \frac{d}{\ell^2} d_i \Delta u_i + \frac{1}{u_0} R_i(u_0 u). \quad (3.1)$$

By the latter equation we deduce that the characteristic diffusion time scale is  $t_0 = \frac{\ell^2}{d}$ . However since we want to focus the attention on the deposition process we will make a different choice of  $t_0$  in the following. Substituting the indicated scalings into (2.2), we obtain

$$-\frac{d}{\ell} d_i \nabla u_i \cdot n = a(a_i u_i - \frac{bv_0}{au_0} b_i v). \quad (3.2)$$

Similarly for equation (2.3), we get:

$$\frac{v_0}{t_0} \partial_t v = u_0 a \sum_{i=1}^N (a_i u_i - \frac{bv_0}{au_0} b_i v). \quad (3.3)$$

Based on (3.3), we take as characteristic deposition time scale  $t_0 = \frac{v_0}{au_0}$ . This is the time scale that we choose to non-dimensionalize the equations.

Thus the moving boundary condition (2.6) becomes

$$\frac{\ell^2}{t_0} r r' = \frac{v_0 \ell}{2\pi t_0 \rho} \int_{\Gamma(r)} \partial_t v. \quad (3.4)$$

Such a moving boundary condition is sometimes referred to as *kinetic condition*.

Here are the equations grouped together after choosing the deposition time scale:

$$\partial_t u_i = \frac{dv_0}{\ell^2 a u_0} d_i \Delta u_i + \frac{v_0}{a u_0^2} R_i(u_0 u) \text{ in } Y - B(r), \quad (3.5)$$

$$-d_i \nabla u_i \cdot n = \frac{a\ell}{d} (a_i u_i - \beta_i v) \text{ on } \Gamma(r) \quad (3.6)$$

$$\partial_t v = \sum_{i=1}^N (a_i u_i - \beta_i v) \text{ on } \Gamma(r) \quad (3.7)$$

$$r r' = \frac{v_0}{2\pi \ell \rho} \int_{\Gamma(r)} \partial_t v \text{ in } Y - B(r). \quad (3.8)$$

We also denote  $\alpha := \frac{v_0}{2\pi \ell}$  and  $\beta := \frac{bv_0}{au_0} \sum_{i=1}^N b_i = \sum_{i=1}^N \beta_i$ , for  $\beta_i := \frac{bv_0}{au_0} b_i$ . To simplify the writing we also change notation  $\tilde{R}_i(u) := \frac{v_0}{a u_0^2} R_i(u_0 u)$  and finally drop the tilde. Due to the structure of the reaction terms, we have the dimensional parameters  $\frac{v_0}{a} \alpha_{i,j} \beta_{i,j}$  and  $\frac{v_0}{a} \alpha_{k,i} \beta_{k,i}$  in front of the factors  $u_i u_j$  and  $u_k u_i$ , respectively. Additionally, we introduce

$$\kappa := \frac{dv_0}{\ell^2 a u_0}$$

as the *surface Thiele modulus*, i.e. the ratio of the deposition rate (seen as surface reaction) over the diffusion rate; see [16] for more on Thiele-like moduli and related Damköhler numbers.

**3.2. Scaling the geometry.** We build the porous material by replicating the information at the patch level  $Y$  until covering perfectly  $\Omega^2$ . We assume that  $\varepsilon := \frac{a\ell}{d}$  is a small positive number. Indeed we have for example  $\varepsilon \simeq 7.61e - 7$  for values given in [20], ( $\ell = 0.101$  m,  $d = 1.8735e - 06$  m<sup>2</sup>/sec,  $a = 1.411e - 11$  m/sec).

Note that  $\Omega^\varepsilon$  is modelled as a composite periodic structure with  $\varepsilon > 0$  the small scale parameter. We also assume that the ratio of microscopic and macroscopic length scales,  $\frac{d}{\ell} = O(\varepsilon)$ .

The latter also indicates that our asymptotics will be connected to a parameter regime where  $\ell \propto \frac{d}{\sqrt{a}}$  as well as that  $a = \varepsilon \frac{d}{\ell} = O(\varepsilon^2)$ .

We consider a periodic array of cells made of scaled identical patches labeled  $Y$ . Scaling this patch by  $\varepsilon$  defines our standard (homogenization) cell. Translating this standard cell in space covers the porous medium  $\Omega$ . For convenience of notation, we write down  $r$  as  $r^\varepsilon$  pointing out this way the dependence of  $r$  on  $\varepsilon$ .

Let  $k = (k_1, k_2) \in \mathbb{Z}^2$  be a vector of indices and  $\{e_1, e_2\}$  be unit vectors in  $\mathbb{R}^2$ . For  $X \subset Y$ , we denote by  $X^k$  the shifted subset  $X^k = X + \sum_{i=1}^2 k_i e_i$ . Using the shifted subset notation, the set  $\Omega_0^\varepsilon = \cup\{\varepsilon Y_0^k : Y_0^k \subset \Omega^\varepsilon\}$  represents the array of pores (voids), while  $\Gamma^\varepsilon = \partial\Omega_0^\varepsilon$  represents the pores boundary. We describe the skeleton of the porous matrix in  $\Omega$  by  $\Omega^\varepsilon = \Omega \setminus \bar{\Omega}_0^\varepsilon$ . Also the boundary of the cells of the periodic domain is the set  $\Gamma_e = \cup\{\varepsilon\partial Y^k\}$ . In these terms, the colloidal species can be either mobile,  $u^\varepsilon$ , hosted in  $\Omega_0^\varepsilon$ , or immobile,  $v^\varepsilon$ , sedimented on  $\Gamma^\varepsilon = \Gamma^\varepsilon(r^\varepsilon)$ .

Finally, we obtain the following set of nondimensionalized equations valid in the locally periodic domain  $\Omega^\varepsilon$  :

$$\partial_t u_i^\varepsilon = \kappa d_i \Delta u_i^\varepsilon + R_i(u^\varepsilon) \quad \text{in } \Omega_0^\varepsilon, i \in \{1, \dots, N\}, \quad (3.9)$$

$$-d_i \nabla u_i^\varepsilon \cdot n_\varepsilon = \varepsilon(a_i u_i^\varepsilon - \beta_i v^\varepsilon) \quad \text{on } \Gamma^\varepsilon, \quad (3.10)$$

$$\partial_t v^\varepsilon = \sum_{i=1}^N a_i u_i^\varepsilon - \beta v^\varepsilon \quad \text{on } \Gamma^\varepsilon, \quad (3.11)$$

$$r^\varepsilon r^{\varepsilon'} = \alpha \int_{\Gamma^\varepsilon(r^\varepsilon)} \partial_t v^\varepsilon \quad \text{in } \Omega_0^\varepsilon. \quad (3.12)$$

The boundary condition at the cell boundary  $\Gamma_e$  is

$$-d_i \nabla u_i^\varepsilon \cdot n_\varepsilon = 0, \quad \text{on } \Gamma_e. \quad (3.13)$$

As initial conditions we take

$$u_i^\varepsilon(0, x) = u_i^0(x), \quad \text{in } \Omega_0^\varepsilon, i \in \{1, \dots, N\}, \quad (3.14)$$

$$v^\varepsilon(0, x) = v^0(x), \quad \text{on } \Gamma^\varepsilon, \quad (3.15)$$

$$r^\varepsilon(0) = r^0. \quad (3.16)$$

The precise definition of  $n_\varepsilon$  will be done in Section 4. Mind that the sets  $\Omega_0^\varepsilon$  and  $\Gamma^\varepsilon$  depend explicitly in time via their dependence on  $r^\varepsilon(t)$ .

Note that the free boundary condition (3.12) assumes both a small growth speed and a maximum radius  $r$  (i.e.  $r < \varepsilon/2$  see cf. [21]). We will show in Section 5 how

---

<sup>2</sup>This is an assumption. In general, pavements with squares can cover perfectly only regions  $\Omega$  that are rectangles. General shapes of  $\Omega$  can only be approximately covered, with a certain controllable error if  $\partial\Omega$  is sufficiently smooth.

to relax this restriction by using the upscaling technique by A. Lacey (see [22], e.g.). Additionally, it is worth mentioning that this  $\varepsilon$ -dependent free boundary problem (FBP) is expected to be locally weakly solvable (up to the time that the free boundary remains a circle) for any fixed value of the small parameter  $\varepsilon > 0$ ; we refer the reader to Appendix A for our arguments.

**4. Locally periodic homogenization.** The geometry of our locally periodic structure is described in Figure 4.1. Our upscaling arguments from this section follow

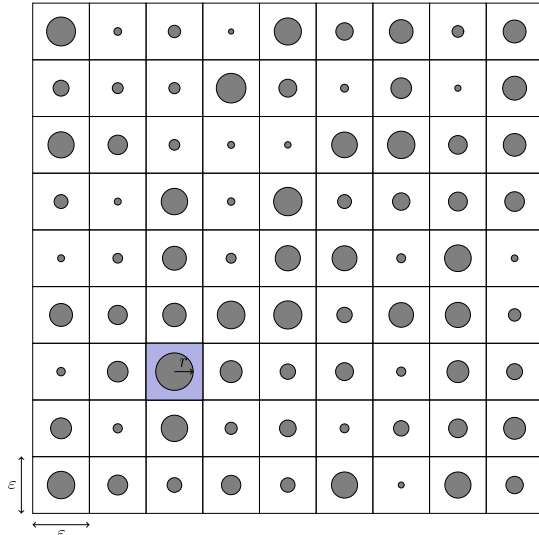


FIG. 4.1. *Locally periodic pore geometry at time  $t = 0$ . The “pores” are balls positioned at  $x \in \Omega$  with radius  $r(x) > 0$ .*

the lines of [15] and [37]. It is worth pointing out that a rigorous justification of the homogenization asymptotics can be obtained for a given distribution of radii  $r(t, x)$  (i.e.  $r(t, x)$  is fixed and not part of the problem as in here, in equation (3.12)) in terms of the concept of  $\theta - 2$  convergence of Alexandre (compare [2]) or using an adaptation of the two-scale convergence designed by G. Nguetseng and G. Allaire to the case of locally periodic functions as in [34] (see references cited therein). Related ideas appear in the context of parabolic equations with rapidly pulsating perforations; see e.g. Ch. 3, Sect. 17 in [8].

Taking  $y = \frac{x}{\varepsilon}$  as the fast variable, we assume the following formal expansion (in terms of  $Y$ -periodic functions) to hold:

$$u_i^\varepsilon(x, y) = u_i^0(x, y) + \varepsilon u_i^1(x, y) + \varepsilon^2 u_i^2(x, y) + \dots \quad (4.1)$$

Noting that  $\nabla = \nabla_x + \frac{1}{\varepsilon} \nabla_y$  and substituting the expansion (4.1) into equation (3.9), we obtain:

$$\begin{aligned} \partial_t(u_i^0 + \varepsilon u_i^1 + \varepsilon^2 u_i^2) = & \kappa(\nabla_x + \frac{1}{\varepsilon} \nabla_y) \cdot \left[ d_i(\nabla_x + \frac{1}{\varepsilon} \nabla_y)(u_i^0 + \varepsilon u_i^1 + \varepsilon^2 u_i^2) \right] \\ & + R_i(u^0 + \varepsilon u^1 + \varepsilon^2 u^2) + \mathcal{O}(\varepsilon^3). \end{aligned} \quad (4.2)$$

Here  $u^j = (u_1^j, u_2^j, \dots, u_N^j)$ ,  $j = 0, 1, 2, \dots$ . Note also that in our case we have a uniform growing of the perforations, so we are targeting only isotropic situations; see the geometry of  $\Omega_0^\varepsilon$  as well as Figure 1 of [20].

We also apply the same formal expansion for the normal vector, pointing out of the surface  $\Gamma^\varepsilon(r(x, t))$ , i.e.

$$n_\varepsilon(t, x, y) = n^0(t, x, y) + \varepsilon n^1(t, x, y) + \mathcal{O}(\varepsilon^2), \quad (4.3)$$

where  $t$  is just a parameter in the structure of  $n^0$  and  $n^1$ ; see e.g. [7] or [15] for the precise analytical expressions of  $n^0$  and  $n^1$  provided that the form of the free boundary is known *a priori*.

Substituting (4.1) and (4.3) into the boundary condition (3.10) yields:

$$-d_i(\nabla_x + \frac{1}{\varepsilon}\nabla_y)(u_i^0 + \varepsilon u_i^1 + \varepsilon^2 u_i^2) \cdot (n^0 + \varepsilon n^1) = \varepsilon(a_i(u_i^0 + \varepsilon u_i^1 + \varepsilon^2 u_i^2) - \beta b_i v) + \mathcal{O}(\varepsilon^3). \quad (4.4)$$

By balancing the terms proportional to  $\varepsilon^{-2}$  in (4.2) and then those proportional to  $\varepsilon^{-1}$  in (4.4), we obtain

$$\kappa \nabla_y \cdot (d_i \nabla_y u_i^0) = 0, \quad (4.5)$$

$$-d_i \nabla_y u_i^0 \cdot n^0 = 0. \quad (4.6)$$

Solving (4.5)-(4.6) results in  $u_i^0 = u_i^0(x)$ , i.e.  $u_i^0$  is constant in the  $y$  variable.

The corresponding terms for  $\varepsilon^{-1}$  in (4.2) and  $\varepsilon^0$  in (4.4) give

$$\kappa \nabla_y \cdot (d_i \nabla_y u_i^1) = 0, \quad (4.7)$$

$$-\nabla_y u_i^1 \cdot n^0 = \nabla_x u_i^0 \cdot n^0. \quad (4.8)$$

Note that the term  $\nabla_y u_i^0 \cdot n^0$  in equation (4.8) is omitted since  $u_i^0 = u_i^0(x)$ .

Denote by  $w := (w_1, w_2)$  the vector of *cell functions*. The components  $w_j$  ( $j \in \{1, 2\}$ ) are solving the following *cell problems*:

$$-\nabla_y \cdot (d_i \nabla_y w_j) = 0, \quad (4.9)$$

$$\nabla_y w_j \cdot n^0 = e_j \cdot n^0, \quad (4.10)$$

where  $\{e_1, e_2\}$  is the orthonormal basis in  $\mathbb{R}^2$ . To pick a concrete unique solution to this Neumann problem, just fix the mean of the solution. Then the following representation holds:

$$u_i^1(x, y) = w(y) \cdot \nabla_x u_i^0(x) + \varphi_i(x), \quad (4.11)$$

where  $\varphi_i$  are given  $y$ -independent functions. Finally, collecting the terms multiplying  $\varepsilon^0$  in (4.2) and then those multiplying  $\varepsilon^1$  in (4.4) lead to:

$$\partial_t u_i^0 = d_i \Delta_x u_i^0 + d_i \nabla_x \cdot \nabla_y u_i^1 + \nabla_y \cdot (d_i (\nabla_x u_i^1 + \nabla_y u_i^2)) + R_i(u^0), \quad (4.12)$$

with

$$-d_i \nabla_x u_i^1 \cdot n^0 - d_i \nabla_y u_i^2 \cdot n^0 - d_i \nabla_x u_i^0 \cdot n^1 - d_i \nabla_y u_i^1 \cdot n^1 = (a_i u_i^0 - \beta_i v) \quad \text{on } \Gamma^\varepsilon \quad (4.13)$$

$$-d_i \nabla_x u_i^1 \cdot n^0 - d_i \nabla_y u_i^2 \cdot n^0 - d_i \nabla_x u_i^0 \cdot n^1 - d_i \nabla_y u_i^1 \cdot n^1 = 0 \quad \text{on } \Gamma_e, \quad (4.14)$$

due to (4.8).



Integrating (4.12) over  $Y(x, t)$ , we obtain:

$$\begin{aligned} \int_{Y(x,t)} \partial_t u_i^0 &= \int_{Y(x,t)} d_i \Delta_x u_i^0 + \int_{Y(x,t)} d_i \nabla_x \cdot \nabla_y u_i^1 + \int_{Y(x,t)} \nabla_y \cdot (d_i (\nabla_x u_i^1 + \nabla_y u_i^2)) \\ &+ \int_{Y(x,t)} R_i(u^0). \end{aligned} \quad (4.15)$$

In the latter equation we have assumed that the domain of quantities such as  $u_i$ , are extended with zero value, inside the solid core of the cell  $Y_0$ .

The terms in (4.15) that do not depend on  $y$  can be taken out from the integral. Remark the presence of the factor  $|Y(x, t)|$ . This is in fact intimately linked with the concept of *total porosity* of the material (see [4]). Since the area of the periodic cell is 4 (for a cell  $[-1, 1] \times [-1, 1]$ ), we have  $|Y(x, t)| = 4$  and  $|Y_0(x, t)| = 4 - \pi r(x, t)^2$ . Then the classical concept of porosity is

$$\phi(x, t) := \frac{|Y_0(x, t)|}{|\Omega|} = \frac{4 - \pi r(x, t)^2}{|\Omega|},$$

where  $|\Omega|$  is the measure (area) of  $\Omega$ . In the following we denote by  $A(x, t) := |Y_0(x, t)|$  the active area of the distributed microstructures.

It is worth noting that dividing (4.15) by  $|\Omega|$  brings in as natural factor the (total) volumetric porosity  $\phi(x, t)$ ; the obtained upscaled equation resembles what one expects in standard textbooks on porous media [4]. In Section 5, since we are interested in capturing macroscopically surface effects due to the motion of the microscopic free boundaries, we prefer to focus on where the area factor  $A(x, t)$  enters the upscaled model equations. Note also that regarding the reaction term,  $R_i(u^0)$ , application of the asymptotic analysis results to first order terms, lead to an expression of exactly the same form as (2.4). Moreover, since  $Y_0 = Y_0(r(x, t)) = Y_0(r)$  and  $A(x, t) = 4 - \pi r(x, t)^2 = \phi(x, t)|\Omega|$ ,  $r = r(v)$ , we now have the implicit relation  $A = A(v)$ . Looking at (3.11), after the averaging process (see also equation (5.1h)) we see that we have  $\tilde{v} := \int_{\Gamma} v_0$  as the accumulated mass of macroscopic immobile species. Interestingly, we observe that in the fast reaction limit  $\kappa \rightarrow +\infty$  the macroscopic system becomes elliptic. More specifically, we have  $\kappa = \frac{dv_0}{\ell^2 a u_0} = \frac{1}{\varepsilon} \frac{v_0}{u_0 \ell}$  and in the case that  $\frac{v_0}{u_0 \ell} = O(1)$  we obtain the aforementioned limiting case. If this is the case, then the derivation of the macroscopic equations can be done in with exactly the same way, resulting in with the elliptic version of equation (5.1h), while the rest of the model equations maintain their form.

This limiting case corresponds in fact to a very fast deposition scenario.

**5. Upscaling extensions for large  $r$ .** Summarizing the results from the previous section, we obtain the following equations for the macroscopic scale :

$$\begin{aligned} \partial_t u_i^0(x, t) &= D_{ijk}(x, t) \Delta_x u_i^0(x, t) + R_i(u^0) \\ &- \frac{L(x, t)}{A(x, t)} (a_i u_i^0(x, t) - \beta_i v_0(x, t)), \end{aligned} \quad (5.1a)$$

describing the diffusion of  $u_i$  in the macroscopic domain. The effective diffusion tensor has the form

$$D_{ijk}(x, t) = d_i \phi(x, t) \tau_{jk}(x, t),$$

where the entries

$$\tau_{jk}(x, t) = \int_{Y(x, t)} (\delta_{j, k} + \nabla_{y_j} w_k(z, t)) dz,$$

build the tortuosity tensor for all  $i = 1, \dots, N$ ,  $j, k = 1, 2$ . In addition

$$L(x, t) = \int_{\Gamma(x, t)} ds = 2\pi r(x, t), \quad A(x, t) = \int_{Y_0(x, t)} dy = 4 - \pi r^2(x, t), \quad (\text{in 2D}) \quad (5.1b)$$

$$R_i(u) = \frac{1}{2} \sum_{i+j=k} \alpha_{i, j} \beta_{i, j} u_i^0 u_j^0 - u_k^0 \sum_{i=1}^{\infty} \alpha_{k, i} \beta_{k, i} u_i^0. \quad (5.1c)$$

Here, our cell functions  $w := (w_1(x, y, t), w_2(x, y, t))$ , assumed to have constant mean, satisfy

$$-\Delta_y w_i = 0, \quad i = 1, 2 \quad \text{in } Y_0(x, t), \quad (5.1d)$$

$$-n_0(x, t) \cdot \nabla_y w_i = 0, \quad \text{on } \Gamma_e, \quad -n_0(x, t) \cdot \nabla_y w_i = n_i(x, t), \quad \text{on } \Gamma(x, t). \quad (5.1e)$$

with  $\Gamma_e := \partial Y$  being the boundary of the cell  $n_0(x, t) = (n_1(x, t), n_2(x, t))$  is the corresponding normal vector. Equation (5.1a) need to be complemented with corresponding initial and boundary conditions. In the sequel of this section, we focus the discussion on the case of a one dimensional macroscopic domain, i.e.  $x \in [0, 1]$ . We set

$$u_i^0(0, t) = \begin{cases} u_i^b > 0 & t \in [0, t_0], \\ 0 & t > t_0, \end{cases}, \quad u_{i, x}^0(1, t) = 0, \quad (5.1f)$$

$$u_i^0(x, 0) = u_i^a(x) \geq 0. \quad (5.1g)$$

We will discuss in Section 6 a couple of concrete choice of suitable initial and boundary conditions.

Moreover we have

$$\partial_t v_0(x, t) = \sum_{i=1}^N \alpha_i u_i^0(x, t) - \beta v_0(x, t), \quad (5.1h)$$

describing the rate of deposition, with some initial condition

$$v_0(x, 0) = v_a(x) \geq 0, \quad (5.1i)$$

and

$$r(x, t) \partial_t r(x, t) = \alpha \left( \sum_{i=1}^N a_i u_i^0(x, t) - \beta v_0(x, t) \right) L(x, t), \quad (5.1j)$$

together with some initial distribution

$$r(x, 0) = r_a(x) > 0, \quad 0 < x < 1, \quad (5.1k)$$

If perforations do not degenerate, i.e.  $0 < r(x, t) < 1$  so pores do not touch, then it holds

$$\partial_t r(x, t) = 2\pi\alpha \left( \sum_{i=1}^N a_i u_i^0(x, t) - \beta v_0(x, t) \right). \quad (5.2)$$

Relation (5.2) describes the rate of increase of the bulk of the immobile core inside a cell centred at the macroscopic position  $x \in \Omega$  at time  $t$ . In our case, regarding equation (5.1a) for a one-dimensional macroscopic consideration,  $D_{ijk}$  and  $\tau_{jk}$  take simpler forms as for instance,  $D_{ijk} = D_i = \kappa d_i \left( 1 + \frac{1}{A(x, t)} \int_{Y(x, t)} \frac{\partial w_1}{\partial y_1} dy \right)$ .

The factor  $\frac{L(x, t)}{A(x, t)}$  appears in (5.1a) as well as in (5.1j) when this is multiplied by  $A(x, t)$ . It can be seen as an effective reaction constant incorporating a surface porosity factor. All these considerations are in agreement with what one would expect while applying directly the macroscopic laws of porous media theory, usually discovered by arguments at REV level involving volume averaging techniques and integral closure relations; see, [4], e.g.

The system of equations (5.1) is assumed to apply for a one-dimensional macroscopic domain (while the related microscopic problem is two-dimensional) with Dirichlet boundary conditions at one side and Neumann boundary conditions at the other side. However, other kind of macroscopic boundary conditions can be also adopted.

In addition, equation (5.1j) applies for a two-dimensional square cell as far as  $0 \leq r \leq 1$ . In order to derive an equation for  $r$  in the case that we have  $r > 1$  for a two-dimensional cell or even a three dimensional one, we have to go back to the original law behind the derivation of equation (5.1j). More precisely, we have that

*Rate of increase of the volume occupied by the immobile species  $\propto$  Rate of change of deposition of the colloidal mass.*

If the volume occupied by the immobile species located at  $x \in \Omega$  is denoted with  $\mathcal{V}(x, t)$ , then we have

$$\partial_t \mathcal{V}(x, t) = \alpha \int_{\Gamma(x, t)} \partial_t v, \quad (5.3)$$

where here the constant  $\alpha = \frac{1}{\rho} > 0$ .

*Two-dimensional cell.* As  $r(x, t)$  reaches 1, it touches  $\partial Y(x, t)$ . At this point, we are concerned with the question: *How does the moving interface  $\Gamma(x, t)$  intersect the cell boundary  $\partial Y(x, t)$ ?* One way to proceed is to assume that the sides of the cell are always tangent to the moving boundary  $\Gamma(x, t)$  as this evolves. This is the case of the *configuration A* (see [22]). Another option is to consider that the moving boundary is always a part of a circle with radius  $r(x, t)$ ,  $1 \leq r(x, t) \leq \sqrt{2}$  and that  $\Gamma(x, t)$  intersects with  $\partial Y$  at some angle. This is the case of *configuration B* (see [22] for calculation details and general playthrough as developed for the classical Stefan problem). We refer the reader also to the (remotely resembling) setting described in [14].

Moreover, we emphasize that here we assume that clogging takes place when  $r$  becomes  $\sqrt{2}$ . We have in mind that according to this modelling scenario we still have diffusion in the direction vertical to the cell plane for  $1 \leq r \leq \sqrt{2}$ . This geometrical approach can be justified if we consider inside the material, a solid skeleton consisting of long narrow cylindrical bars equispaced and parallel (see Figure 5.1).

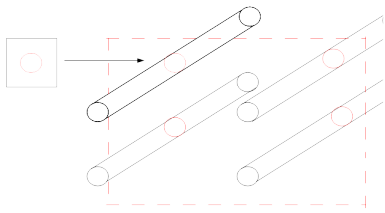


FIG. 5.1. Schematic representation of a plane crosssecting parallel bars of a solid skeleton. A square on that plane containing the cross section, a circle in this case, centred in it can be considered as one cell in our model.

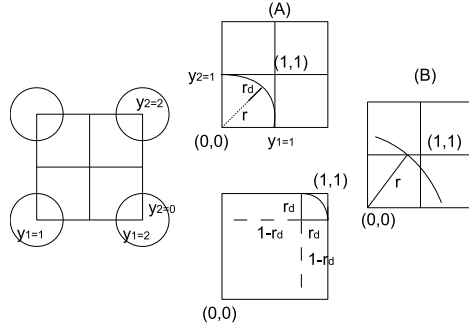


FIG. 5.2. Schematic representation of configurations A and B. In configuration A we have constant zero angle between the cell boundary and the interface while in configuration B the angle of the tangent of the interface and the cell boundary varies as the interface evolves.

Then we may think of a plane intersecting these cylinders transversely and obtain a sequence of equispaced circular segments corresponding to the solid parts, while the rest of the plane corresponds to a net of voids. Next taking advantage of this symmetrical setting we consider square cells filling the plane with each one of them containing a solid segment centred in it while the rest is void. Also, the symmetrical growth of the solid core inside the cell allows us instead of using the standard periodic conditions at the exterior boundary  $\Gamma_e$ , to use Neumann conditions as in the first of (5.1e).

*Configuration A.* We assume that  $1 \leq r(x, t) \leq \sqrt{2}$  is the line segment, part of the diagonal of the square (line segment from  $(0, 0)$  to  $(1, 1)$  in Figure 5.2) with end points  $(0, 0)$  and the point of intersection of the diagonal with the free boundary  $\Gamma(x, t)$ . In such a case the free boundary will be a quarter of a circle with radius say  $r_d = r_d(x, t)$ . Then  $r(x, t)$  and  $r_d(x, t)$  are related in the following way

$$(r(x, t) - r_d(x, t)) + \sqrt{2}r_d(x, t) = \sqrt{2}. \quad (5.4)$$

Thus

$$r_d(x, t) = \frac{\sqrt{2} - r(x, t)}{\sqrt{2} - 1}, \quad r'_d(x, t) = -\frac{1}{\sqrt{2} - 1}r'(x, t).$$

In addition, the area occupied by the immobile species will be equal to 4 times the square quarter minus the square of size  $r_d(x, t)$  plus the quarter of the circle with radius  $r_d(x, t)$ . This gives

$$\mathcal{V}(x, t) = 4 \left[ 1 - r_d^2(x, t) + \frac{1}{4}\pi r_d^2(x, t) \right] = 4 \left[ 1 + r_d^2(x, t) \left( \frac{\pi}{4} - 1 \right) \right].$$

Therefore the rate of change of the area in terms of  $r_d(x, t)$  is

$$\partial_t \mathcal{V}(x, t) = 8 \left( \frac{\pi}{4} - 1 \right) r_d(x, t) r'_d(x, t) = \alpha \int_{\Gamma(x, t)} v_t.$$

In terms of  $r(x, t)$ , the latter relation reads

$$\partial_t \mathcal{V}(x, t) = 8 \frac{\left(1 - \frac{\pi}{4}\right)}{(\sqrt{2} - 1)^2} (\sqrt{2} - r(x, t)) r'(x, t) = \alpha \int_{\Gamma(x, t)} v_t,$$

where  $\bar{\alpha} = \alpha \frac{(\sqrt{2}-1)^2}{8(1-\frac{\pi}{4})}$  such that

$$(\sqrt{2} - r(x, t))r'(x, t) = \bar{\alpha} \int_{\Gamma(x, t)} v_t$$

holds. Consequently, the equation (5.1j) from the original system needs to be replaced by

$$\partial_t r(x, t) = \begin{cases} \frac{1}{r(x, t)} \alpha \left( \sum_{i=1}^N a_i u_i^0(x, t) - \beta v_0(x, t) \right) L(x, t), & r_a \leq r \leq 1, \\ \frac{1}{\sqrt{2}-r(x, t)} \bar{\alpha} \left( \sum_{i=1}^N a_i u_i^0(x, t) - \beta v_0(x, t) \right) L(x, t), & 1 \leq r \leq \sqrt{2}, \end{cases}$$

for

$$L(x, t) = \begin{cases} 2\pi r(x, t), & r_a \leq r \leq 1, \\ 2\pi r_d(x, t) = 2\pi \frac{\sqrt{2}-r(x, t)}{\sqrt{2}-1}, & 1 \leq r \leq \sqrt{2}, \end{cases}$$

and

$$A(x, t) = 4 - \mathcal{V}(x, t) = \begin{cases} 4 - \pi r^2(x, t), & r_a \leq r \leq 1, \\ 4(1 - \frac{\pi}{4}) \left( \frac{\sqrt{2}-r(x, t)}{\sqrt{2}-1} \right)^2, & 1 \leq r(x, t) \leq \sqrt{2}. \end{cases}$$

*Configuration B.* The free boundary consists here of four arcs of a circle of radius  $r(x, t)$ , with  $1 \leq r(x, t) \leq \sqrt{2}$ . In this case the area of the immobile species will be equal to 4 times the volume of the two triangles plus the circular sector corresponding to angle  $\frac{\pi}{2} - 2 \cos^{-1}(\frac{1}{r})$ . More specifically, we have

$$\mathcal{V}(x, t) = 4 \left[ \sqrt{r(x, t)^2 - 1} + \frac{r(x, t)^2}{2} \left( \frac{\pi}{2} - 2 \cos^{-1}\left(\frac{1}{r(x, t)}\right) \right) \right].$$

Then the rate of change of the immobile species area will be

$$\partial_t \mathcal{V}(x, t) r(x, t) = \frac{d}{dt} \left[ 4 \sqrt{r(x, t)^2 - 1} + r(x, t)^2 \left( \pi - 4 \cos^{-1}\left(\frac{1}{r(x, t)}\right) \right) \right] = \alpha \int_{\Gamma(x, t)} v_t(x, t),$$

or

$$2r(x, t) \left( \pi - 4 \cos^{-1}\left(\frac{1}{r(x, t)}\right) \right) r'(x, t) = \alpha \int_{\Gamma(x, t)} v_t.$$

In such a case

$$\partial_t r(x, t) = \begin{cases} \frac{1}{r(x, t)} \alpha \left( \sum_{i=1}^N a_i u_i^0(x, t) - \beta v_0(x, t) \right) L(x, t), & r_a \leq r(x, t) \leq 1, \\ \gamma(x, t) \left( \sum_{i=1}^N a_i u_i^0(x, t) - \beta v_0(x, t) \right) L(x, t), & 1 \leq r(x, t) \leq \sqrt{2}, \end{cases}$$

with

$$\gamma(x, t) := \frac{\alpha}{2r(x, t) \left( \pi - 4 \cos^{-1}\left(\frac{1}{r(x, t)}\right) \right)}$$

$$L(x, t) = \begin{cases} 2\pi r(x, t), & r_a \leq r(x, t) \leq 1, \\ r(x, t) \left[ 2\pi - 8 \cos^{-1}\left(\frac{1}{r(x, t)}\right) \right], & 1 \leq r(x, t) \leq \sqrt{2}, \end{cases}$$

and, finally,

$$A(x, t) = 4 - \mathcal{V}(x, t) = \begin{cases} 4 - \pi r^2(x, t), & r_a \leq r \leq 1, \\ 4 \left[ 1 - \sqrt{r^2(x, t) - 1} + r^2(x, t) \left( \frac{\pi}{4} - \cos^{-1}\left(\frac{1}{r(x, t)}\right) \right) \right], & 1 \leq r(x, t) \leq \sqrt{2}. \end{cases}$$

**6. Numerical approximation.** To treat numerically problem (5.1), we need firstly to obtain a good numerical approximation for the cell problems (5.1d) and determine the shape of the cell functions  $w_1, w_2$  posed in  $Y_0(x, t)$ . More specifically, we proceed for the various values of  $r$ , at a first stage for  $r_a \leq r(x, t) \leq 1$  and, at a second stage, for  $1 < r(x, t) \leq \sqrt{2}$  depending which microscopic configuration (A or B) is considered. We take a partition of width  $\delta r$ ,  $r_a = r_0, r_1 = r_0 + \delta r, \dots, r_{M_1} = 1$ . Then since  $Y_0$  is determined as the area contained inside the square cell and outside the circle of radius  $r$ , we obtain a sequence of solutions for each  $Y_{0_i}$  corresponding to the radius  $r_i$  of the partition. In the same way, for a partition of the interval  $[1, \sqrt{2}]$ ,  $1 = r_{M_1+1}, \dots, r_M = \sqrt{2}$  we solve again the problem in the domain the way that this is specified in the case of configuration A or B. Note that in these cases the domain  $Y_0$  is reduced into four separate segments and thus we need the solution (due to symmetry) in only one of them. Then we use a finite element scheme to solve these cell problems. The finite element numerics package in MATLAB "Distmesh" ([31]) is used to triangulate the domain  $Y_{0_i} = Y_0(r_i)$  and a solver that has been implemented for this specific problem (equations (5.1d)) is applied.

We illustrate the numerical solution for this problem for specific choices of  $r_i$ ; see Figure 6.1 for  $r_i = .5$  and Figure 6.2 for  $r_i = 1.2$  and configuration A, and for  $r_i = 1.1$  and configuration B.

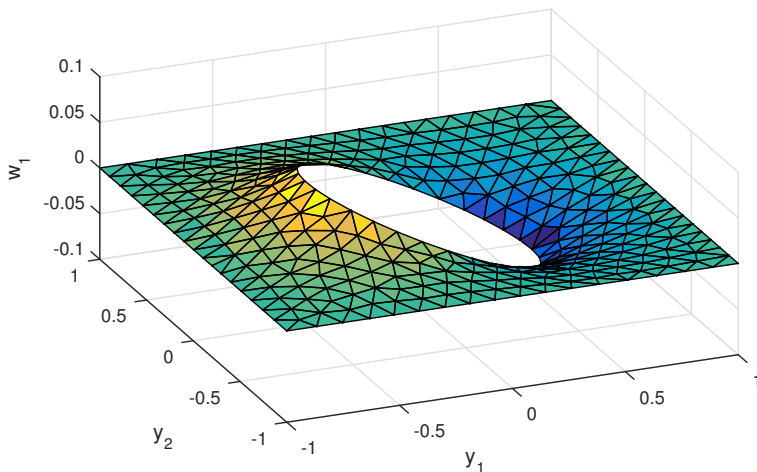


FIG. 6.1. Numerical solution of the cell problem (5.1d) and specifically for  $w_1$  with  $r_i = .5$ .

Having available the numerical evaluation of the cell functions  $w$  as approximate solutions to the cell problems (5.1d) and (5.1e), the entries of the diffusion tensor  $D_{ijk} = \int_{Y_0(x, t)} d_i (\delta_{j, k} + \nabla_{y_j} w_k)$ ,  $i = 1, \dots, N$ ,  $j, k = 1, 2$  can be calculated directly.

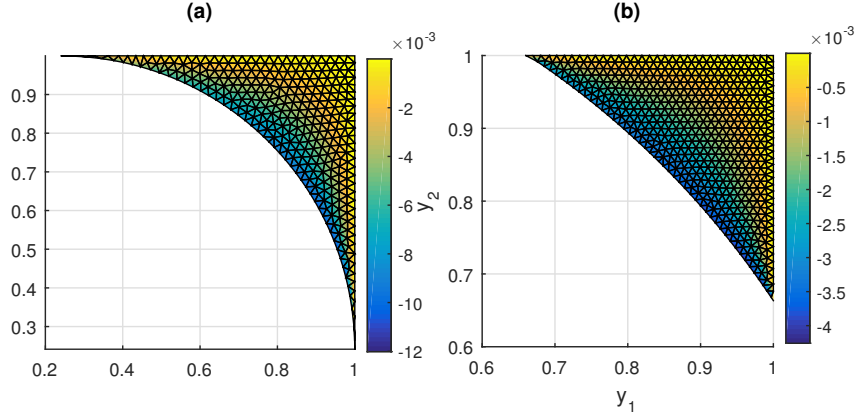


FIG. 6.2. Numerical solution of the cell problem (5.1d): The profile of  $w_1$  for (a) the configuration A and for (b) the configuration B.

More specifically, for each  $(x, t)$  and consequently for each  $Y_0(x, t)$ , the corresponding value of  $D_{ijk}(x, t)$  is approximated via linear interpolation. For the cases that  $0 < r(x, t) < 1$ ,  $(4 - \pi \leq |Y_0(x, t)| \leq 4)$  as well as for  $1 < r(x, t) < \sqrt{2}$  and configurations A and B, the results regarding the diagonal entries, needed for equation (5.1a), are shown in Figure 6.3.

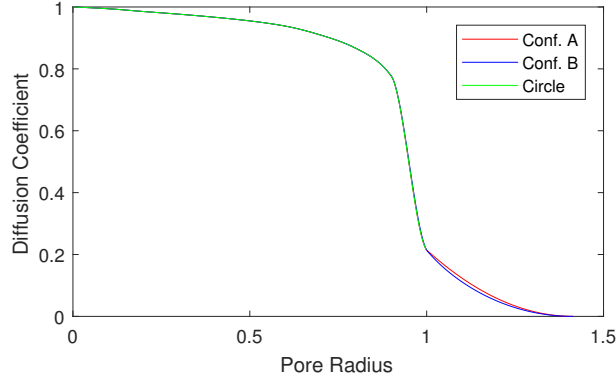


FIG. 6.3. The diffusion matrix dependence on the choice of the pore radius.

Next, we solve the system of equations (5.1a)-(5.1k). We use a finite element scheme to solve the one-dimensional version of the field equation (5.1a), together with its boundary and initial conditions. Let  $\psi_j = \psi_j(r)$ ,  $j = 0, \dots, M$  denote the standard linear B - splines defined on the interval  $[0, 1]$  with respect to the considered partition.

We then take the Galerkin approximation  $u_i(x, t) = \sum_{j=0}^M a_{u_{ij}}(t)\psi_j(x)$ ,  $v(x, t) = \sum_{j=0}^M a_{v_j}(t)\psi_j(x)$   $\tau \geq 0$ ,  $0 \leq r(x, t) \leq 1$ . We also take  $r(x, t) = \sum_{j=0}^M a_{r_j}(t)\psi_j(x)$  for  $r$  in (5.1j). Applying the standard Galerkin method, we obtain a system of equations for the coefficients  $a_{u_{ij}}(t)$ ,  $a_{v_j}(t)$ ,  $a_{r_j}(t)$ ,  $i = 1, \dots, N$ ,  $j = 1, \dots, M$ . The resulting system of ODE's is finally solved by an implicit time-stepping scheme.

**Finite element scheme for the model equations.** We substitute the above expressions of  $u_i(x, t)$ ,  $v(x, t)$  and  $r(x, t)$  in equation (5.1) multiply with  $\psi_l$  and then integrate over  $[0, 1]$  to obtain

$$\begin{aligned} \sum_{j=0}^M \dot{a}_{u_{i_j}} \int_0^1 \psi_j \psi_l dx &= \kappa d_i \sum_{j=0}^M a_{u_{i_j}} \int_0^1 D(x, t) \psi_j' \psi_l' dx + \int_0^1 R \left( \sum_{j=0}^M a_{u_{i_j}} \psi_j \right) \psi_l dx \\ &\quad - (\alpha_i a_{u_{i_j}} - \beta_i a_{v_j}) \int_0^1 \frac{L(x, t)}{A(x, t)} \psi_j \psi_l dx \end{aligned} \quad (6.1)$$

where  $l = 1, 2, \dots, M$  and the dot, “ $\cdot$ ”, denotes differentiation with respect to time. Similarly, for equation (5.1h), we have

$$\sum_{j=0}^M \dot{a}_{v_j} \int_0^1 \psi_j \psi_l dx = \sum_{i=1}^N \alpha_i \sum_{j=0}^M a_{u_{i_j}} \int_0^1 \psi_j \psi_l dx - \beta \sum_{j=0}^M a_{v_j} \int_0^1 \psi_j \psi_l dx. \quad (6.2)$$

Finally, for equation (5.1j) it holds

$$\sum_{j=0}^M \dot{a}_{r_j} \int_0^1 \psi_j \psi_l dx = 2\pi\alpha \left( \sum_{i=1}^N \alpha_i \sum_{j=0}^M a_{u_{i_j}} \int_0^1 \psi_j \psi_l dx - \beta \sum_{j=0}^M a_{v_j} \int_0^1 \psi_j \psi_l dx \right). \quad (6.3)$$

Setting  $a_{u_i} := [a_{u_{i_1}}, a_{u_{i_2}}, \dots, a_{u_{i_M}}]^T$  and  $a_v := [a_{v_1}, a_{v_2}, \dots, a_{v_M}]^T$ , the system of equations for the coefficients  $a_{u_i}$ 's takes then the form

$$B_l \dot{a}_{u_i}(t) = B_r(t) a_{u_i}(t) + b_R(t) - C(t) (\alpha a_{u_i}(t) - \beta a_v(t)),$$

with  $t \in (0, T]$ .

The corresponding FEM matrices are

$$B_l := \left( \int_0^1 \psi_j(x) \psi_l(x) dx \right), \quad B_r := \kappa d_i \left( \int_0^1 D(x, t) \psi_j'(x) \psi_l'(x) dx \right),$$

$$C := \left( \int_0^1 \frac{L(x, t)}{A(x, t)} \psi_j(x) \psi_l(x) dx \right),$$

while  $b_R(t)$  is the array with entries  $b_R(t) := \int_0^1 R \left( \sum_{j=0}^M a_{u_{i_j}} \psi_j \right) \psi_l dx$ .

What concerns the equation of  $v$  we have

$$B_l \dot{a}_v(t) = \left( \sum_{i=1}^N \alpha_i B_l (\alpha a_{u_i}(t) - \beta a_v(t)) \right),$$

while for  $r$  we get

$$B_l \dot{a}_r(t) = 2\pi \left( \sum_{i=1}^N \alpha_i B_l (\alpha a_{u_i}(t) - \beta a_v(t)) \right).$$



Next, we apply an implicit in time scheme of the form

$$[B_l - \delta t B_r(t_n) + \delta t \alpha C(t_n)] a_{u_i}^{n+1} - \delta t \beta C(t_n) a_v^{n+1} = B_l a_{u_i}^n + \delta t b_R(t_n), \quad (6.4)$$

$$a_{u_i}^{n+1} - \delta t \left( \sum_{i=1}^N \alpha_i (\alpha a_{u_i}^{n+1} - \beta a_v^{n+1}) \right) = a_{u_i}^n, \quad (6.5)$$

$$a_r^{n+1} - \delta t 2\pi \left( \sum_{i=1}^N \alpha_i (\alpha a_{u_i}^{n+1} - \beta a_v^{n+1}) \right) = a_r^n, \quad (6.6)$$

for  $\delta t$  the time step and  $t_n = (n-1)\delta t \in [0, T]$ ,  $n \in \{1, \dots, [T/\delta t]\}$ , to solve the system numerically.

**7. Discussion of simulation results.** To obtain a couple of relevant simulation examples, we choose the following set of parameter values: We consider  $N = 3$  mobile species  $u_i$  and one immobile species.

We take  $\kappa = 1$ ,  $(d_1, d_2, d_3) = (.3, .5, .99)$ ,  $(a_1, a_2, a_3) = (.9, .5, .3)$ ,  $(\beta_1, \beta_2, \beta_3) = (1, 1, 1)$ ,  $(u_1^b, u_2^b, u_3^b) = (1, 1, 1)$ ,  $\alpha_{i,j} = .1$ ,  $\beta_{i,j} = 100$ ,  $i, j = 1, \dots, 3$ ,  $u_a^i(x) = 0$ ,  $v_a(x) = 0$ ,  $r_a(x) = .1$ ,  $0 \leq x \leq 1$ . Finally, the generation of mass at the boundary  $x = 0$  is traced up to time  $t_0 = 2$ . At this particular instant, we also observe a relevant jump in the form of the  $u_i$ 's (cf. the next simulations). For all these simulations, the reference parameters are chosen in the range indicated in [20].

**7.1. Basic output. Detecting clogging regions.** The basic simulation output is shown in Figure 7.1. This is done for configuration A, where the mass of the various components of the system, i.e.  $U_i(t) = \int_0^1 u_i(x, t) dx$ ,  $V(t) = \int_0^1 v(x, t) dx$ , is plotted against time.

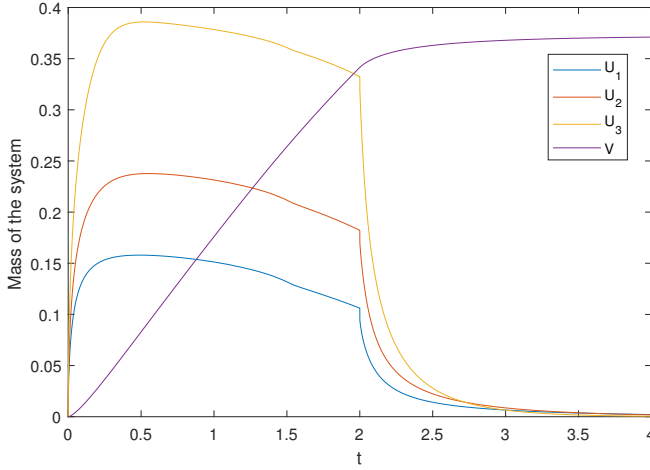


FIG. 7.1. Mass of the system against time for the various colloidal species in the system

If we decrease the value of the parameters  $\beta_{i,j}$ , the collision kernel expressing the ability of the particles to aggregate, and for instance take them to be uniformly constant  $\beta_{i,j} = 1$ , then (after the time that  $u_i(0, t)$  becomes zero) the decay of the  $U_i$ 's is moderate due to the fact that the aggregation mechanism now is weaker. This is shown in Figure 7.2.

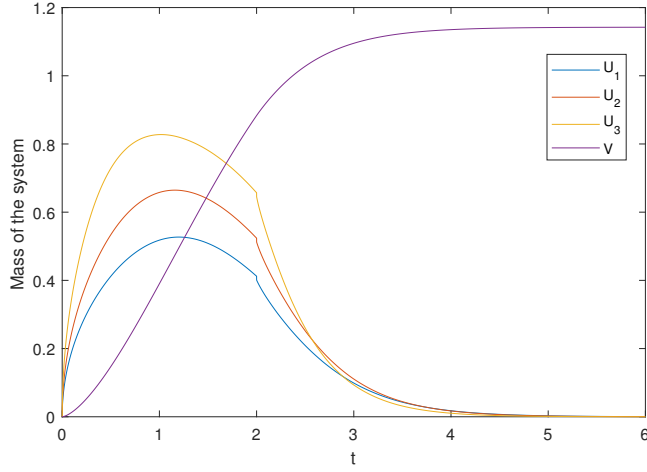


FIG. 7.2. Mass of the system against time for the various colloidal species in the system.

Increasing the number of mobile species yields similar results. As an example, for  $N = 5$  mobile species the simulation is demonstrated in the following Figure 7.3. The parameter values used here are the same as those used in the previous simulation in Figure 7.1 for the first three species,  $i = 1, 2, 3$ . More specifically, we take  $(d_1, d_2, d_3, d_4, d_5) = (.3, .5, .99, .2, .3)$ ,  $(a_1, a_2, a_3, a_4, a_5) = (.9, .5, .3, .4, .3)$ ,  $(\beta_1, \beta_2, \beta_3, \beta_4, \beta_5) = (1, 1, 1, 1, 1)$ ,  $(u_1^b, u_2^b, u_3^b, u_4^b, u_5^b) = (1, 1, 1, 1, 1)$ . The proximity of the variables  $u_1$  and  $u_4$ , and also of  $u_2$  and  $u_5$  in Figure 7.3 is due to the particular (arbitrary) choice of the diffusion coefficients  $d_i$ 's and the  $a$ 's.

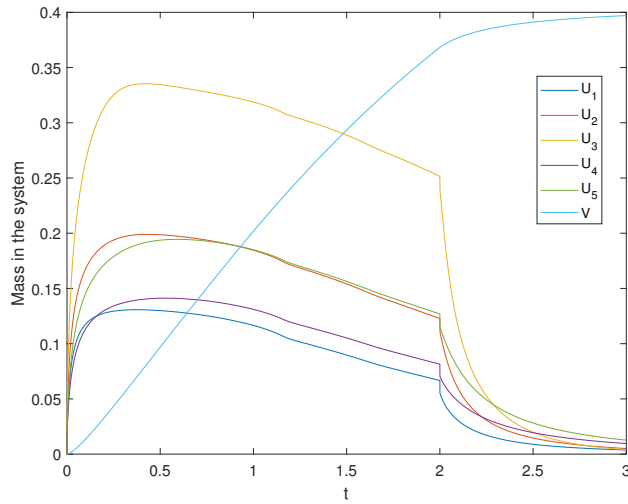


FIG. 7.3. Mass of the system against time for the various components of the system in the case of 5 mobile species

In the same simulation we can also observe the evolution of the free boundary

inside the cells at the point  $x = 0$ . More precisely, in the next set of figures, we see the evolution of the core consisting of immobile species for a sequence of time steps. In Figure 7.4 this effect is shown for the case that configuration A is assumed. As far as  $r(x, t) < 1$  the core has a cyclic form and then for later times the corners of the cell are gradually filled by the immobile species with its boundary cyclic and tangential to the cell boundary. Similarly for the configuration B, the evolution of the moving

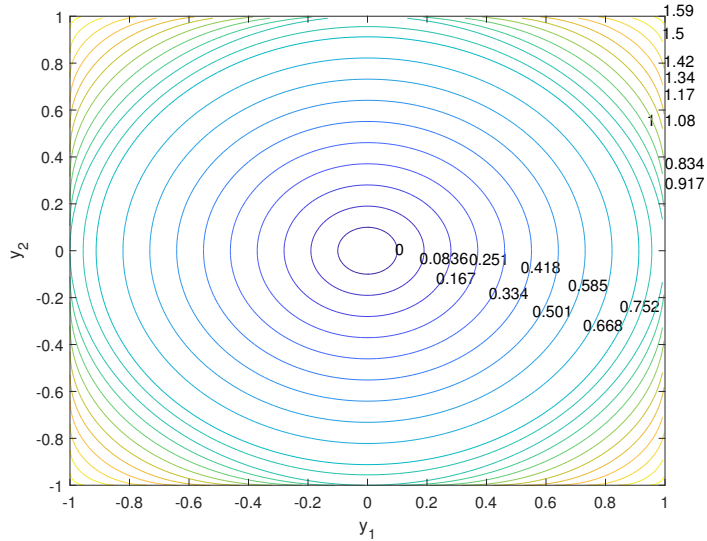


FIG. 7.4. Evolution of the moving boundary of the core formed by the immobile species for the case of configuration A at the point  $x = 0$ . The numbers upon the curves indicate the time.

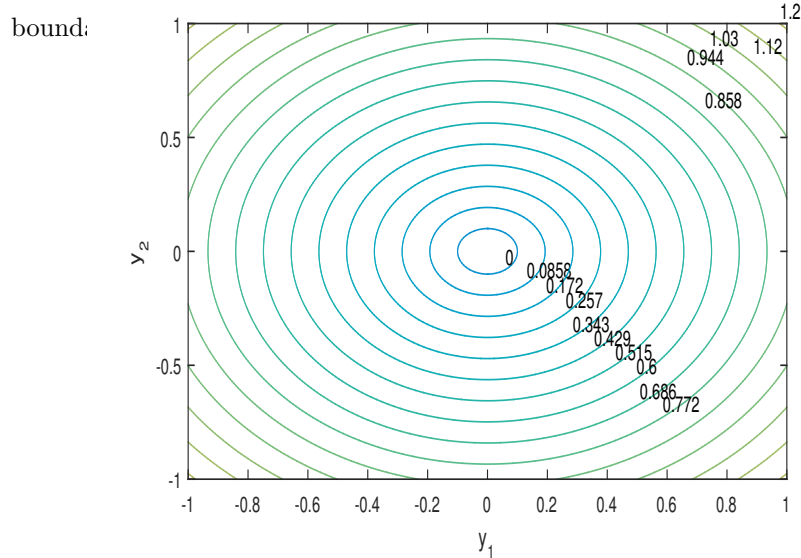


FIG. 7.5. Evolution of the moving boundary of the core formed by the immobile species for the case of configuration B. The numbers upon the curves indicate the time.

The numbers that are used in these graphs, Figures 7.4 and 7.5, are the same as

those used in producing Figure 7.1.

Furthermore, in the next Figure 7.6 a simulation is presented for various values of the surface Thiele modulus  $\kappa$ . Keeping the mass constant at the left boundary  $x = 0$  with increased  $\kappa$  ( $\kappa = 10$ ), we have more mass supply in the system and therefore higher values for  $U_i$ 's and  $V$ . The opposite effects is apparent for lower  $\kappa$ , ( $\kappa = 0.1$ ).

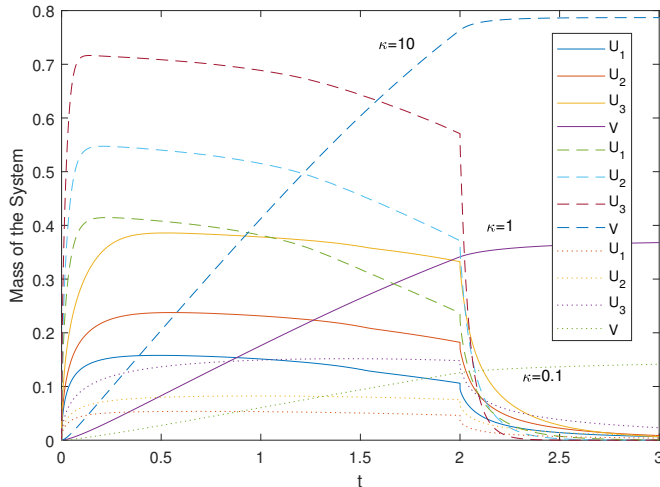


FIG. 7.6. Plot of the system mass,  $U_i$ 's and  $V$ ,  $i = 1, 2, 3$ , for various values of  $\kappa$ , (a)  $\kappa = 10$  (dashed lines), (b)  $\kappa = 1$  (solid lines), (c)  $\kappa = 0.1$  (dotted lines). The rest of the parameters are the same as in Figure 7.1.

Finally, a comparison with the same model but with constant diffusion, the same for all species, is shown in Figure 7.7. Here we can observe that for the same species when we consider variable diffusion coefficient, decreased with time, we have less amount of species diffusing inside the bulk of the material and therefore the total mass of the species is smaller compared with the case that we run the same simulation but with constant diffusion. When the supply from the left boundary stops at time  $t_0 = 2$ , then the remaining mobile species collide to the core and finally the mass of the system in both cases evens out (in the sense the  $u_i$ 's and  $V$  tend to a steady state). This behaviour seems to be robust.

Moreover, the porosity evolution is apparent in Figure 7.8. The porosity function  $\phi(x, t)$  is plotted here against time for certain values of the variable  $x$  for  $r(x, 0) = .88$  ( $\phi(x, 0) \simeq 0.39$ ) and with the rest of the values as in Figure 7.1. The porosity decay is much faster close to  $x = 0$  and actually becomes zero at time  $t \simeq 1.22$  which means that we have clogging at that point and any boundary condition there does not effect any more the rest of the domain. Additionally, due to the latter fact, almost immediately after clogging the system settles down to stationary state, close to that state observed at clogging time, since now we have the same problem with no flux condition at both boundaries.

In the following set of simulations shown in Figure 7.9, we investigate the effect of non-uniform initial pore radii distribution, i.e.  $r(x, 0) = r_a(x)$  (non constant). For the first simulations, we take  $r(0, t) = x^2$  and for the case when configuration A is assumed (red dashed line). The radius  $r(x, t)$  is plotted for time  $t = t_p = 2.5$  for  $t_p = \frac{5}{6}T$  ( $[0, T]$  is the simulation interval with  $T = 3$ ) against  $x$  (red solid line). Note

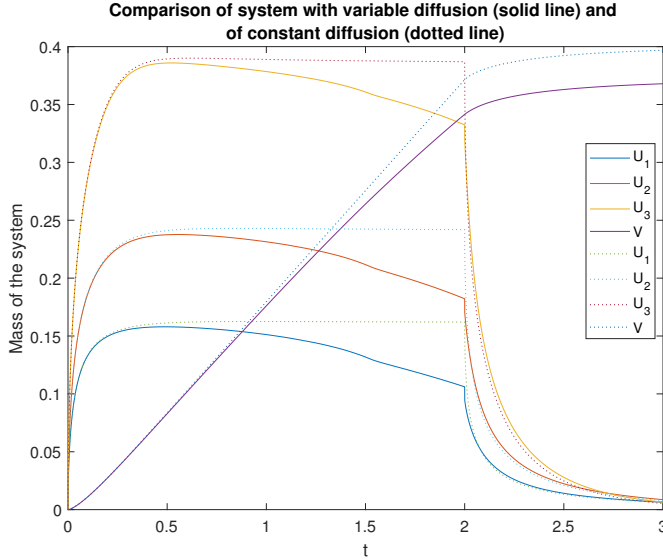


FIG. 7.7. The breakthrough curve comparison for constant diffusion vs. pore-growth diffusion. We can observe an initial agreement in both cases and then a decrease in the case of variable (due to pore growth) diffusion which is the result of the decreasing diffusion coefficient. However, after time  $t = 2$ , where the boundary condition is dropped to zero the profile evens out to match the one of the larger constant diffusion.

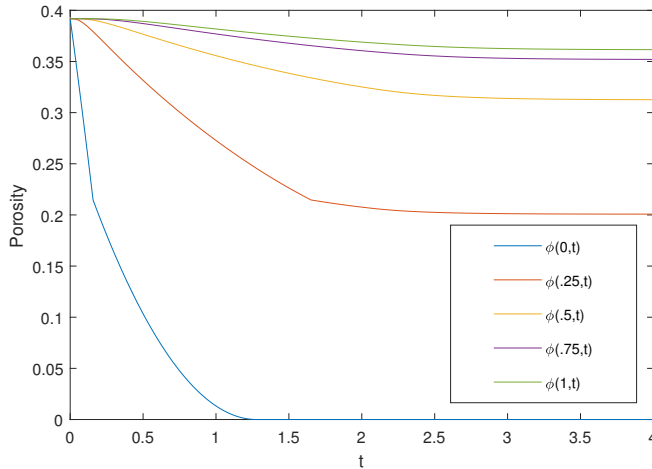


FIG. 7.8. Plot of porosity  $\phi(x, t)$  against time  $t$  at certain points  $x_i$  in the domain  $[0, 1]$ .

that the time  $t_p$  is chosen appropriately at each of the following simulations so that to capture the clogging behaviour of the system We have clogging when  $r$  reaches  $\sqrt{2}$  at some point and this threshold is denoted by the black line. When  $r$  reaches  $\sqrt{2}$  at some point  $x_0$  then the pores in that point are clogged and we have no mobility from the area  $x < x_0$  to the area  $x > x_0$ . For this case this happens initially at the point  $x = 0$ .

Changing the initial distribution of  $r$  by taking now  $r(x, 0) = r_0 x^2$  for  $r_0 = 1.38$  close to  $\sqrt{2}$ , we may have a situation that the whole domain is almost clogged simultaneously ( blue line in Figure 7.9).

Finally, we obtain an interesting situation if we take the values of  $r(x, 0)$  at the points of the partition given by a random distribution. In this case starting with a

normal distribution with mean 0.3 and variance 0.8 we obtain at time  $t_p$  a profile (green line) in which clogging is exhibited at the points  $x \simeq 0, 0.1, 0.5, 0.6, 0.9$ . Also for this case and this specific time step  $t_p$ , at certain selected points  $x_i$ , a schematic image of a square cell is plotted together with circle of radius  $r(x_i, t_p)$ . Starting with a continuous uniform (rectangular) distribution in the interval  $[0, \sqrt{2}]$  we obtain a similar result.

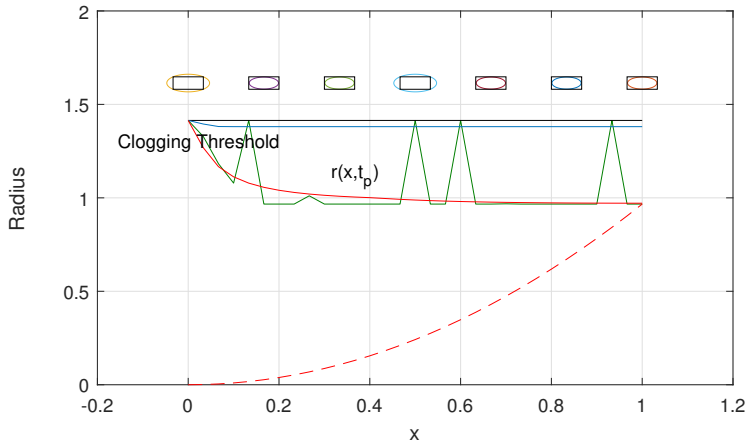


FIG. 7.9. Form of radius distribution at time  $t_p = 2.5$  for the case that we take (i)  $r(x, 0) = x^2$  (red dashed line), (ii)  $r(x, 0) = 1.38x^2$ , (iii) random normal distribution with mean 0.3 and variance 0.8. The radius  $r(x, t_p)$  is plotted for these cases with (i) red line, (ii) blue line, (iii) green line. In the latter case at the top of the graph a schematic image of some square cell is plotted together with corresponding circle of radius  $r(x_i, t_p)$ .

The occurrence of clogging can be seen in these graphs when  $r(x, t_p)$  reaches  $\sqrt{2}$  at some point  $x$  and time  $t_p$ . Now, one could also ask: *How can one distinguish between through-pores and ink-bottled pores?* Our current level of understanding is that if  $r$  is lower than 1, then we have through-pores, while for  $r > 1$  we have bottle-through pores. Looking at Figure 7.9, we see that (at a fixed time slice) the clogging threshold is reached in a number of points (e.g.  $x = 0.5$  and  $x = 0.6$ ). In this region we expect blind and closed pores to appear<sup>3</sup>.

A similar experiment is demonstrated in Figure 7.10 but for the case of configuration B. The initial distribution here is taken to be linear  $r(x, 0) = x$  and here  $t_p = 2$ . In the top of the figure we can see the state of the cells at this time step. Since material is inserting from point  $x = 0$ , clogging takes place initially there and then we see no significant variation in the evolution of the process at later times.

Based on the numerical results shown in Figure 7.8, Figure 7.9 and Figure 7.10, we conjecture the following:

<sup>3</sup> From a catalysis-oriented perspective, e.g. cf. [25], pores can be closed (not accessible from the air parts of the pore matrix), blind (open at only one end), or through (open at both ends). Each pore can be isolated or, more frequently, connected to other pores to form the porous network. The irregular shape of the pores and their connectivity cause a molecule or a colloidal particle to cover a distance greater than the grain size when passing through the porous material.

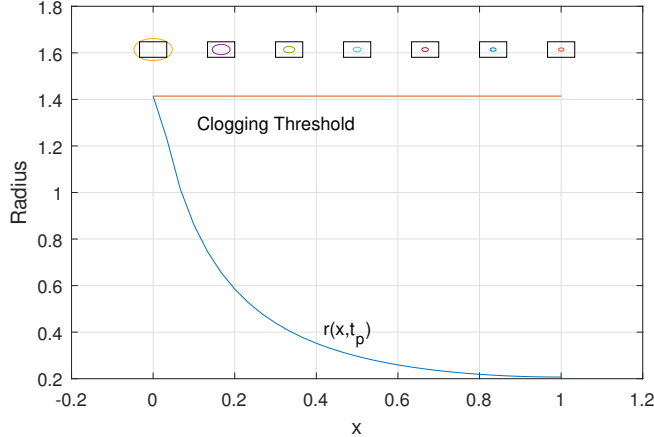


FIG. 7.10. Form of radius distribution  $r(x, t_p)$  at time  $t_p = 2$  for the case of configuration B and having initially  $r(x, 0) = x$ . We observe clogging at the point  $x = 0$ . At the top of the graph, a schematic image of square cells centered at the points  $x_i = (i - 1)h$ ,  $h = 0.142$ ,  $i = 1 \dots 7$ , is plotted together with the corresponding circle of radius  $r(x_i, t_p)$ .

If ink-bottle pores are clogged, then the storage capacity of the material reaches a certain saturation threshold simultaneously with a potential increase of the averaged transport up to a maximum level. On the other hand, if through pores become clogged, then the averaged transport is decreased leading to a raise in the storage capacity.

In Section 7.2, we bring in some further partial support for this conjecture, by estimating numerically the mass of colloids that have deposited on the pores surfaces and were not depleted from there during a given time interval.

**7.2. A posteriori estimation of the storage capacity.** A major question related to modern porous media applications is how much  $\text{CO}_2$ , energy, colloids, residual nuclear particles etc. can be stored in the fabrics of a given heterogeneous medium; see [26] for instance. If, like in our case, the distribution, shape and volume of the microstructures is controlled, then the storage capacity of the porous medium can be estimated numerically employing the upscaled model equations. Of course, even in our rather simple case, such a task is quite complex especially if one targets accurate estimations. The success depends on a lot of factors such as the space inside the pores available for the colloids to accumulate, the void space inside the pores where colloids feel free to move, number and location of clogging regions, etc. Part of this information is incorporated in our model in the functions  $L(x, t)$  (tortuosity information, in the sense that with increasing  $L$  the average travelling length of a particle in the non-solid part of a cell also increases) and the porosity  $\phi(x, t)$ . In addition to these aspects, additional factors that are not included in this model such as the shape and size of the colloids, the way that they are packed and accumulated in the pore surface etc. should be taken into account if one wants a better insight. On top of this, due to the nonlinearity and coupling in the upscaled system, we cannot aim to determine a specific formula of the storage capacity of the system. However, in our context we can give an estimation in an indirect way. If we focus at a point of our domain at time  $t = 0$  we may consider that it has minimum storage capacity. As the system evolves with time, the pores associated to this macroscopic spatial point tend to fill out, so more matter (colloids) can be stored in the system. We refer to this scenario as an increase in the storage capacity of the medium until the time

where clogging occurs. Then the capacity reaches a threshold. The latter means that we have no void space or free surface at this point i.e. the pores are either vanished or closed and hence additional storage becomes impossible. Based on such picture, we can define a local capacity storage indicator as well as a global capacity storage indicator by exploiting the difference  $SC_\ell(x_c, t) = (v(x_c, t) - v(x_c, 0))$ , where  $x_c$  is the point where clogging occurs.

Also, for the case that at time  $t = 0$  we have a uniform initial distribution of pore radii and since the geometry in the microstructure is considered uniform, for any another point say  $x$  (even when not clogging occurs there) we expect that we should have the same maximum storage capacity  $v(x_c, T)$  and its (local) storage capacity at time  $t$  should be  $SC_\ell(x, t) = v(x, t) - v(x, 0)$ . A global indicator of the capacity storage is then  $SC_g(t) = \int_{\Omega} (v(x, t) - v(x, 0)) dx$ .

To get further insight, in the numerical experiment shown in Figure 7.10, we extend the inflow at the boundary  $x = 0$  for timeslot  $[0, t_0]$ ,  $t_0 = 3$  (cf. (5.1f)) so that enough mass is inserted in the system allowing us to observe clogging at the point  $x = 0$ . In Figure 7.11, the local storage capacity indicator  $SC_\ell(x, t)$  is plotted vs. time for various choices of spatial points  $x$ . The thick line in the picture represents the global storage capacity indicator vs. time. In the next plot (see Figure 7.12) the

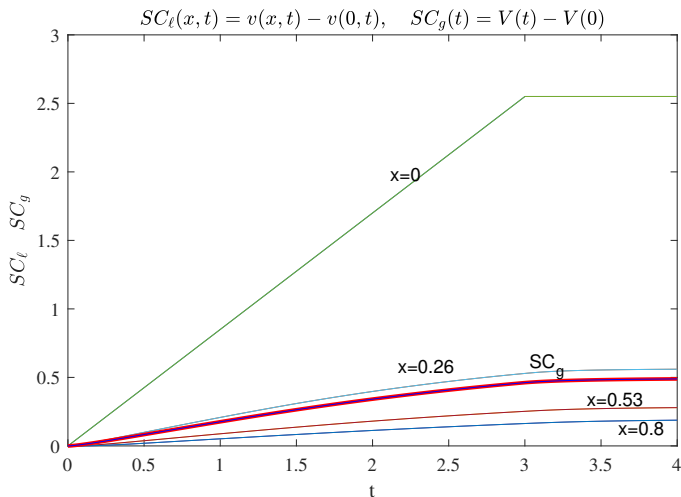


FIG. 7.11. Estimation of the local and global storage capacity indicators as functions of time, where  $V(t) = \int_{\Omega} v(x, t) dx$ .

pore radius  $r(x, t)$  (left) and the concentration of the immobile  $v(x, t)$  (right) species are plotted against time for the same choice of spatial points. The similarity between the two behaviors points out the fact that we expect that any eventual closed form formula for a storage indicator should incorporate a suitable monotonic dependence on the pore radii. More investigations are needed to shed light on this effect. One could also wonder what would be the effect of an additional curvature term like  $-\alpha \frac{1}{r(x, t)}$  ( $\alpha > 0$ ) in the definition of the speed of the microscopic free boundaries. Interestingly, our simulations show that, for both configurations A and B, the storage capacity of the porous medium increases in the sense that more mass is stored in the system compared with the no-curvature case; see Figure 7.13 for an illustration of what happens in the case of configuration A; for configuration B a similar result can



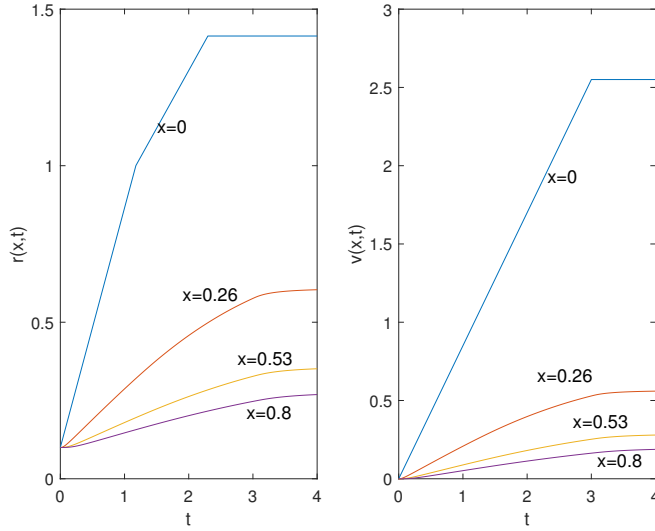


FIG. 7.12. The pore radius  $r(x, t)$  and the concentration profile  $v(x, t)$  are plotted with respect to time for  $x = 0, 0.26, 0.53, 0.8$ .

be pointed out. To understand why and how this effect occurs, one needs to study the time evolution of more types of shapes, preferably less regular and non-symmetrical, but this goes beyond our aim here.

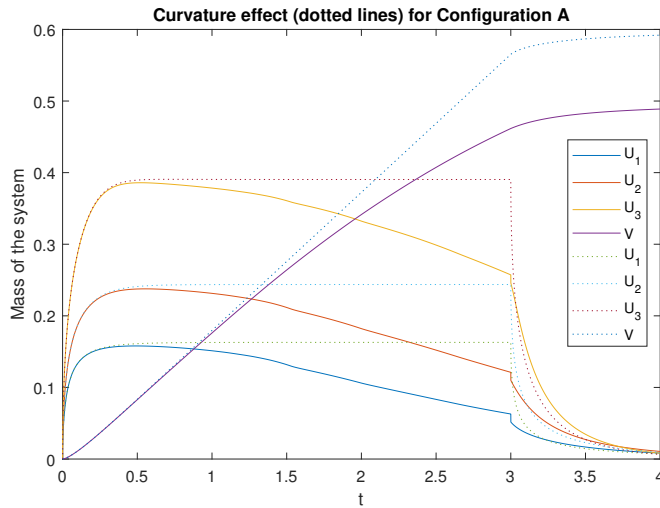


FIG. 7.13. Total mass in the system for configuration A, when the term  $-\alpha \frac{1}{r(x,t)}$ ,  $\alpha = 0.1$  is added to the equation of  $r'(x, t)$  as given by (2.6).

## 8. Conclusions.

A few conclusions can be drawn for this framework: If the internal structure of a porous material is fixed with respect to time, then the effective transport and storage properties of the material can usually be sufficiently well estimated by empirical measurements. Efficient mathematical averaging methodologies are needed to deliver realistic quantitative estimations of the transport and storage capacity of heterogeneous materials with evolving internal structures (think of the effect of freezing or thawing ice lenses in cementitious-based materials) - for

such situations, experimental techniques fail to be applicable.

What concerns the choices of microstructures considered here, we have seen that both the volumetric porosity and the surface porosity (i.e. the ratio of the area of the voids in a plane cross section of the porous medium to the total area of the cross section), are proportional to  $A(x, t)$ , the effective reaction constant (via Henry-like exchange) is proportional to  $L(x, t)$ , and the tortuosity as well as the effective diffusion coefficient to  $\left(1 + \frac{1}{A(x, t)} \int_{Y(x, t)} \frac{\partial w_1}{\partial y_1} dy\right)$ . For the simplified setting taken to describe the large radii case,  $w_1$  is a cell function which together with the analytic expressions for  $A(x, t)$  and  $L(x, t)$ , depends on the selected microscopic configuration ( $A$ ,  $B$ , or some other admissible situation).

We do not have a way to express analytically the effective storage capacity of a heterogeneous domain (with or without evolving microstructures!). However, for the particular choices of microstructures chosen here we are able to estimate numerically an averaged transport flux allowing for local reductions eventually due to clogging or to a sudden formation of localized high-density zones induced by the microstructure evolution. Using the evolution equation for the mass of deposited colloids, we can define and compute numerically local and global capacity storage indicators.

If a more complex shape of locally-periodic microstructure needs to be approximated, then a front-tracking approximation scheme (e.g. using a suitable level-set equation) will need to substitute our numerical approach. The same holds if  $\Omega$  is two or three dimensional. Should a 3D setting be treated, then (2.6) has to be changed accordingly. We expect that in this case the estimation of the storage capacity is more difficult to obtain especially if ball-like grains are replaced by other growing shapes.

In spite of the fact the the FBP is well-posed locally in time (cf. Appendix A) and that we have reasons to expect that the macroscopic model is globally well-posed (e.g. trusting the approach from [37, 38]), we are unable at this moment to perform the rigorous homogenization for this setting. The missing ingredient is a lower uniform in  $\varepsilon$  estimate of the local existence time of the oscillating FBP. The weak solvability of the microscopic system can be handled up to the first clogging point. Looking at the macroscopic equations, if clogging occurs transport (elliptic part) degenerates simultaneously with other terms in the upscaled equations. A similar situation has been encountered for clogging pipe-like pores in [43]. In both these scenarios, one lacks a rigorous upscaling of the degenerate evolution equations.

In this framework, we have discussed only the case when convective flows are absent. Further investigations are needed to clarify how flows with moderate oscillatory speeds can be handled in this setting.

**9. Acknowledgments.** The authors thank Dr. Oleh Krehel (Eindhoven) for helpful discussions. AM acknowledges partial financial support from NWO-MPE “Theoretical estimates of heat losses in geothermal wells” (grant nr. 657.014.004) and from Swedish Research Council “Homogenization and dimension reduction of thin heterogeneous layers” (grant nr. 2018-03648).

## Appendix A. Comments on the local weak solvability of the original FBP.

We consider the simplified case when the solid phase in  $\Omega$  consists of a collection of  $M \in \mathbb{N}$  disjoint balls with centers in  $x_\ell \in \Omega$  ( $\ell \in \{1, \dots, M\}$ ) placed on a regular  $\delta$ -grid (see Figure 4.1); the grid’s cells have diameter  $\delta > 0$ . We look into the case when  $0 < \epsilon \ll \delta$  and assume that the centers do not move and the ball-shape is

preserved during the evolution of the free boundary. We fix the notation as follows:

$$\Omega_0^\varepsilon(r_\varepsilon(t)) := \cup_{\ell=1}^M \varepsilon Y_0(x_\ell, r_\ell(t)) \text{ and } \Gamma^\varepsilon(r_\varepsilon(t)) := \cup_{\ell=1}^M \varepsilon \partial Y_0(x_\ell, r_\ell(t)).$$

To simplify the writing, let us refer to  $\Omega_0^\varepsilon(r_\varepsilon(t))$  and to  $\Gamma^\varepsilon(r_\varepsilon(t))$  simply as  $\Omega_0^\varepsilon(t)$  and respectively,  $\Gamma^\varepsilon(t)$ . Consequently,  $\Omega^\varepsilon(t) := \Omega\text{-clos}(\Omega_0^\varepsilon(t))$ ,  $\Omega_T^\varepsilon := \cup_{t \in (0, T)} (\Omega_0^\varepsilon(t) \times \{t\})$ , and  $\Omega_T := \Omega \times (0, T)$  for some  $T > 0$ .

Further, let the maximum existence time interval be denoted by

$$t^{\delta\varepsilon} := \inf\{t : 2\varepsilon r_\ell(t) = \delta, \ell \in \{1, \dots, M\}\}.$$

Note that, by construction, we have  $t^{\delta\varepsilon} > 0$ . Set  $u^\varepsilon = (u_1^\varepsilon, \dots, u_N^\varepsilon)$  for the vector of colloidal populations and  $r^\varepsilon(t) = (r_1^\varepsilon(t), \dots, r_M^\varepsilon(t))$  for the vector of radii of the growing balls.

The FBP we are considering is: Find the triple  $(u_\varepsilon, v_\varepsilon, r_\varepsilon)$  satisfying the following evolution system:

$$\partial_t u_i^\varepsilon = \kappa d_i \Delta u_i^\varepsilon + R_i(u^\varepsilon) \quad \text{in } \Omega_0^\varepsilon(t), i \in \{1, \dots, N\}, \quad (\text{A.1})$$

$$-d_i \nabla u_i^\varepsilon \cdot n_\varepsilon = \varepsilon(a_i u_i^\varepsilon - \beta_i v^\varepsilon) \quad \text{on } \Gamma^\varepsilon(t), \quad (\text{A.2})$$

$$\partial_t v^\varepsilon = \eta \left( \sum_{i=1}^N a_i u_i^\varepsilon - \beta v^\varepsilon \right) \quad \text{on } \Gamma^\varepsilon(t), \quad (\text{A.3})$$

$$r_\ell^\varepsilon(t) r_\ell^\varepsilon(t)' = \alpha \int_{\partial Y_0(x_\ell, \varepsilon r_\ell(t))} \partial_t v^\varepsilon \quad \text{in } \Omega_0^\varepsilon(t), \quad (\text{A.4})$$

endowed with the following boundary and initial conditions

$$\nabla u_i^\varepsilon \cdot n_\varepsilon = 0 \quad \text{on } \partial \Omega_T, \quad (\text{A.5})$$

$$u_i^\varepsilon(0, x) = u_i^0(x) \quad \text{in } \Omega_0^\varepsilon(t), i \in \{1, \dots, N\}, \quad (\text{A.6})$$

$$v^\varepsilon(0, x) = v^0(x) \quad \text{on } \Gamma^\varepsilon(t), \quad (\text{A.7})$$

$$r_\ell^\varepsilon(0) = r_\ell^0, \ell \in \{1, \dots, M\}. \quad (\text{A.8})$$

In (A.3), the function  $\eta : \mathbb{R} \rightarrow [0, \infty)$  defined via  $\eta(s) = s^+$  is taken to ensure jointly with (A.4) that the balls  $Y_0(x_\ell, \varepsilon r_\ell(t))$  can only increase their size in time. The positivity of  $\partial_t v^\varepsilon$  is an essential aspect; it needs either to be imposed by employing  $\eta$ , or it must be proven to hold in a certain parameter regime (using sub- and super-solutions). It is worth mentioning at this point that the rigorous averaging of this setting is in progress. The main challenge is at least twofold: (i) a suitable scaling of the balls as well as a proper dependence  $\delta = \delta(\varepsilon)$  must be identified such that eventual boundary layers arising around the growing surfaces affect the averaging in a controlled way, (ii) the size of the maximum time interval where the local solvability of the FBP can be ensured is depending in an unsuitable way on the choice of  $\varepsilon$ . Especially what concerns (ii), the situation here is totally different compared to the better understood case of Ostwald ripening.

Here, we only sketch the proof idea for the application of the Banach-fixed-point theorem to this setting ensuring local-in-time well-posedness of the FBP. We transform the moving domain  $\Omega_0^\varepsilon(t)$  into the fixed domain  $\Omega_0^\varepsilon(0)$  by some diffeomorphism depending not only on the choice of  $r^\varepsilon(t)$  but also on its regularity and uniform boundedness in suitable norms; see also [3], where the authors have fixed the free

boundaries in a multiple-connected domain related to Ostwald ripening with kinetic undercooling. We refer the reader to [32] where a simple connected domain has been treated.

Take

$$\Phi(\cdot, r^\varepsilon(t)) : \Omega_0^\varepsilon(0) \rightarrow \Omega_0^\varepsilon(t) \text{ given by } \Psi(x, t) = \Phi(x, r^\varepsilon(t)).$$

Herewith, the newly transformed functions are  $\tilde{u}^\varepsilon(x, t) = u^\varepsilon(\Psi(x, t), t)$  and  $\tilde{v}^\varepsilon(x, t) = v^\varepsilon(\Psi(x, t), t)$ . We now make use of the following notation referring to the (active part of the) structure of our heterogeneous medium in the fixed-domain formulation, viz.  $\Omega_T^\varepsilon(0) := \cup_{t \in (0, T)} (\Omega_0^\varepsilon(0) \times \{t\})$ .

Given sufficiently regular  $r^\varepsilon$  and  $\frac{1}{r^\varepsilon}$ , it results that the pair of functions  $(\tilde{u}^\varepsilon, \tilde{v}^\varepsilon)$  must satisfy the parabolic problem

$$\begin{aligned} \sqrt{\det(D\Psi^T D\Psi)} \partial_t \tilde{u}_i^\varepsilon - kd_i \operatorname{div} \left( \sqrt{\det(D\Psi^T D\Psi)} (D\Psi^T D\Psi)^{-1} \nabla \tilde{u}_i^\varepsilon \right) &= R_i(\tilde{u}^\varepsilon) + \\ + \sqrt{\det(D\Psi^T D\Psi)} D\Psi^{-T} \nabla \tilde{u}_i^\varepsilon \partial_t \Psi &\text{ in } \Omega_T^\varepsilon(0) \end{aligned} \quad (\text{A.9})$$

$$\nabla \tilde{u}_i^\varepsilon \cdot n = 0 \text{ at } \partial\Omega_T^\varepsilon(0), \quad (\text{A.10})$$

$$D\Psi^{-T} \nabla \tilde{u}_i^\varepsilon = \varepsilon(a_i \tilde{u}_i^\varepsilon - \beta_i \tilde{v}_i^\varepsilon) \text{ at } \partial\Omega_T^\varepsilon(0), \quad (\text{A.11})$$

$$\begin{aligned} \sqrt{\det(D\Psi^T D\Psi)} \partial_t \tilde{v}^\varepsilon &= \sum_{i=1}^N (a_i \tilde{u}_i^\varepsilon - \beta_i \tilde{v}_i^\varepsilon) + \\ + \sqrt{\det(D\Psi^T D\Psi)} D\Psi^{-T} \nabla \tilde{u}_i^\varepsilon \partial_t \Psi &\text{ at } \partial\Omega_T^\varepsilon(0). \end{aligned} \quad (\text{A.12})$$

Reasoning as in Theorem 4.1 in Ref. [3], standard theory of parabolic regularity ensures that if  $(\tilde{u}_i^\varepsilon(0), \tilde{v}^\varepsilon(0)) \in H^1(\Omega_0^\varepsilon(0))^N \times H^1(\partial\Omega_0^\varepsilon(0))$ ,  $r^\varepsilon \in W_+^{1,\infty}(0, T)^M$ , and  $\frac{1}{r^\varepsilon} \in L^\infty(0, T)$  for all  $\ell \in \{1, \dots, M\}$  and some  $T \in (0, t^{\delta\varepsilon})$ , then problem (A.9)–(A.12) admits a unique solution

$$(\tilde{u}^\varepsilon, \tilde{v}^\varepsilon) \in (L^\infty(0, T; L^2(\Omega_0^\varepsilon(0))) \cap L^2(0, T; H^1(\Omega_0^\varepsilon(0))))^N \times H^1(0, T; L^2(\Omega_0^\varepsilon(0))).$$

The calculation details finally ensuring the local-in-time existence of weak solutions to the FBP are tedious. We only indicate here that the construction of the fixed-point mapping is as follows: Start off with a suitable  $r^\varepsilon$  (i.e.  $r^\varepsilon(t) > 0$  for  $t \in (0, T)$  and  $r^\varepsilon \in W_+^{1,\infty}(0, T)^M$ ) and solve problem (A.9)–(A.12). Insert the obtained solution in the equation obtained by fixing the moving boundary in (A.4). Refer to its solution as  $s^\varepsilon$ . Conclude the argument by proving for pairs of weak solutions an estimate of type  $\int_0^T |s_1^\varepsilon - s_2^\varepsilon|^\nu \leq \lambda \int_0^T |r_1^\varepsilon - r_2^\varepsilon|^\nu$ , where  $\lambda \in (0, 1)$  and  $\nu \in [2, 4]$ . Such an estimate is a typical feature of FBPs for one-dimensional parabolic systems with kinetic conditions at the free boundary and can be extended to higher dimensions only if the symmetry of the evolving domains allow reduction to 1D. It shows that an improved integrability of the free boundary is available and it closes the fixed-point argument. The proof of such estimate relies on fine energy estimates as well as on trace interpolation inequalities combined with integral identities specific to the FBP; see, for instance, the proof of Theorem 3.4 from [28] for handling a specific 1D case and [9] for the 2D case. Using Stampacchia's method in our context, suitable restrictions on data and parameters can be identified so that the obtained weak solutions stay a.e. positive.

## REFERENCES

- [1] T. Aiki, A. Muntean, "Large-time behavior of solutions to a thermo-diffusion system with Smoluchowski interactions." *Journal of Differential Equations*, **263** (5) (2017), 3009–3026.
- [2] R. Alexandre, "Homogenization and  $\theta - 2$  convergence." *Proc. Royal Soc. Edinburgh* **127A**(1997), 441–455.
- [3] D.C. Antonopoulou, G.D. Karali, N.K. Yip, "On the parabolic Stefan problem for Ostwald ripening with kinetic undercooling and inhomogeneous driving force." *Journal of Differential Equations*, **252** (2012), 4679–4718.
- [4] J. Bear, "Dynamics of Fluids in Porous Media.", Dover, 1988.
- [5] I.J. Beyerlein, M.J. Demkowicz, A. Misra, B.P. Uberuaga, "Defect-interface interactions." *Progress in Materials Science* **74** (2015), 125–210.
- [6] M. Bruna, J. Chapman, "Diffusion in spatially varying porous media." *SIAM J. Appl. Math.* **75**(2015), 1648–1674.
- [7] G. A. Chechkin, A. L. Piatnitskii, "Homogenization of boundary-value problems in a locally periodic perforated domain." *Applicable Analysis* **71** (1) (1999), 215–235.
- [8] G. A. Chechkin, A. L. Piatnitskii, A. S. Shamaev, "Homogenization Methods and Applications.", AMS, vol 234. Translations of Math. Monographs, 2007.
- [9] F. Conrad, D. Hilhorst, T. I. Seidman, "Well-posedness of a moving boundary problem arising in a dissolution-growth process.", *Nonlinear Analysis TMA* **15** (1990), 445–465.
- [10] M. P. Dalwadi, I. M. Griffiths, M. Bruna, "Understanding how porosity gradients can make a better filter using homogenization theory." *Proc. R. Soc. A* **471**(2015), 20150464.
- [11] M. P. Dalwadi, I. M. Griffiths, M. Bruna, "A multiscale method to calculate filter blockage." *J. Fluid Mech.* **809**(2016), 264–289.
- [12] C. Eck, "Homogenization of a phase field model for binary mixtures." *SIAM Multiscale Model. Simul.*, **3** (1) (2006), 1–27.
- [13] M. Elimelech, J. Gregory, X. Jia, R. A. Williams, "Particle Deposition and Aggregation: Measurement, Modelling and Simulation.", Elsevier, 1995.
- [14] J. D. Evans, A. Fernandez, A. Muntean, "Single and two-scale sharp-interface models for concrete carbonation—Asymptotics and numerical approximation." *SIAM Multiscale Model. Simul.* **10** (3) (2012), 874–905.
- [15] T. Fatima, N. Arab, E. Zemskov, A. Muntean, "Homogenization of a reaction-diffusion system modeling sulfate corrosion of concrete in locally periodic perforated domains." *Journal of Engineering Mathematics*, **69** (2-3) (2011), 261–276.
- [16] G. F. Froment, G. Bischoff. "Chemical Reactor Analysis and Design." John Wiley & Sons, 2011.
- [17] E. J. Hinch, "Perturbation Methods." *Cambridge University Press*, 1991.
- [18] P. R. Johnson, M. Elimelech, "Dynamics of colloid deposition in porous media: Blocking based on random sequential adsorption." *Langmuir*, **11** (3) (1995), 801–812.
- [19] P. A. Korevaar, S. J. George, A. J. Markvoort, M. M. Smulders, P. A. Hilbers, A. P. Schenning, T. F. De Greef, E. Meijer, "Complexity in supramolecular polymerization" *Nature*, **481**.7382 (2012), 492–496.
- [20] O. Krehel, A. Muntean, P. Knabner, "Multiscale modeling of colloidal dynamics in porous media: Capturing aggregation and deposition effects." *Advances in Water Resources*, **86** (A) (2015), 209–216.
- [21] O. Krehel, "Aggregation and fragmentation in reaction-diffusion systems posed in heterogeneous domains." PhD Thesis, TU Eindhoven, NL, 2015, (DOI: 10.6100/IR780944).
- [22] A. A. Lacey, L. A. Herraiz, "Macroscopic models for melting derived from averaging microscopic Stefan problems I: Simple geometries with kinetic undercooling or surface tension." *Euro. Jnl. of Applied Mathematics*, **11** (2002), 153–169.
- [23] A. A. Lacey, L. A. Herraiz, "Macroscopic models for melting derived from averaging microscopic Stefan problems II: Effect of varying geometry and composition." *Euro. Jnl. of Applied Mathematics*, **13**(2002), 261–282.
- [24] A. Ledesma-Durn, S. I. Hernandez, and I. Santamara-Holek, "Relation between the porosity and tortuosity of a membrane formed by disconnected irregular pores and the spatial diffusion coefficient of the Fick-Jacobs model." *Physical Review E*, **95**, (2017), 052804.
- [25] G. Leofantia, M. Padovan, G. Tozolla, B. Venturelli, "Surface area and pore texture of catalysts." *Catalysis Today* **41** (1-3) (1998), 207–219.
- [26] X. Lou, Wang, Y., Yuan, C., Lee, J., Archer, L. "Template-free synthesis of SnO<sub>2</sub> hollow nanostructures with high Lithium storage capacity." *Adv. Mater.* **18** (1-3) (2006), 2325–2329.
- [27] F. Moro, H. Böhni, "Ink-bottle effect in mercury intrusion porosimetry of cement-based

- materials." *Journal of Colloid and Interface Science*, **246** (1) (2002), 135–149.
- [28] A. Muntean, M. Böhm, "A moving boundary problem for concrete carbonation: Global existence and uniqueness of weak solutions." *Journal of Mathematical Analysis and Applications*, **246** (1) (2009), 234–251.
- [29] C. V. Nikolopoulos, "A model for melting of an inhomogeneous material during modulated temperature differential scanning calorimetry." *Applied Mathematical Modelling*, **28** (5) (2004) 427–444.
- [30] J. M. Nordbotten, M. Celia, "Geological Storage of CO<sub>2</sub> : Modeling Approaches for Large-Scale Simulation." *Wiley*, 2015.
- [31] P. O. Persson, G. Strang, "A simple mesh generator in MATLAB." *SIAM Review*, **46**(2) (1998), 329–345.
- [32] M. A. Peter, M. Böhm, "Multiscale modelling of chemical degradation mechanisms in porous media with evolving microstructure." *SIAM Multiscale Model. Simul.*, **7** (4) (2009), 1643–1668.
- [33] W. Peukert, H.C. Schwarzer, F. Stenger, "Control of aggregation in production and handling of nanoparticles." *Chemical Engineering and Processing*, **44** (2) (2005), 245–252.
- [34] M. Ptashnyk, "Locally periodic unfolding method and two-scale convergence on surfaces of locally periodic microstructures." *SIAM Multiscale Model. Simul.*, **13**(2015), 1061–1105.
- [35] S. Qamar, G. Warnecke, "Numerical solution of population balance equations for nucleation, growth and aggregation processes." *Computers & Chemical Engineering*, **31** (12) (2007), 1576–1589.
- [36] N. Ray, T. van Noorden, F. Frank, P. Knabner, "Multiscale modeling of colloid and fluid dynamics in porous media including an evolving microstructure." *Transport in Porous Media*, **95** (3) (2012), 669–696.
- [37] N. Ray, T. van Noorden, F. A. Radu, W. Friess, P. Knabner, "Drug release from collagen matrices including an evolving microstructure." *ZAMM – Zeitschrift für Angewandte Mathematik und Mechanik*, **93** (10-11) (2013), 811–822.
- [38] N. Ray, T. Elbinger, P. Knabner, "Upscaling the flow and transport in an evolving porous medium with general interaction potentials." *SIAM J. Appl. Math.*, **75** (5) (2015), 2170–2192.
- [39] G. Rimmelé, V. Barled-Gouedard, O. Porcherie, B. Goffe, F. Brunet, "Heterogeneous porosity distribution in Portland cement exposed to CO<sub>2</sub>-rich fluids." *Cement and Concrete Research*, **38** (8-9) (2008), 1038–1048.
- [40] R. Schulz and P. Knabner, "An effective model for biofilm growth made by chemotactical bacteria in evolving porous media." *SIAM J. Appl. Math.*, **77**(2017), 1653-1677.
- [41] M. G. Toledo, K. S. Utria, F. A. Gonzalez, J. P. Zuniga, A. V. Saveliev, "Hybrid filtration combustion of natural gas and coal." *International Journal of Hydrogen Energy*, **37** (8) (2012), 6942–6948.
- [42] B. S. van Lith, A. Muntean, C. Storm, "A continuum model for hierarchical fibril assembly." *EPL (Europhysics Letters)*, **106** (6) (2014), 68004.
- [43] T. van Noorden, "Crystal precipitation and dissolution in a porous medium: Effective equations and numerical experiments." *SIAM Multiscale Model. Simul.*, **7** (2008), 1220–1236.
- [44] K. Wilmanski, "Thermomechanics of Continua." *Springer Verlag*, 1998.
- [45] C. Zhang, Y. Bai, S. Xu, X. Yue, "Homogenization for chemical vapor infiltration process." *Commun. Math. Sci.*, **15** (4) (2017), 1021–1040.
- [46] Y. Zhu, J. Wang, Y. Xiang, X. Guo, "A three-scale homogenisation approach to the prediction of long-time absorption of radiation induced interstitials by nanovoids at interfaces." *Journal of Mechanics and Physics of Solids*, **106** (6) (2014), 68004.